

# Electronic Structure of Activated Bleomycin: Oxygen Intermediates in Heme versus Non-Heme Iron

Frank Neese,<sup>†</sup> Jeffrey M. Zaleski, Kelly Loeb Zaleski, and Edward I. Solomon\*

Contribution from the Department of Chemistry, Stanford University, Stanford, California 94305-5080

Received May 24, 2000. Revised Manuscript Received September 13, 2000

**Abstract:** Bleomycin (BLM) is a glycopeptide antibiotic produced by the fungus *Streptomyces verticillus* which is used clinically for anticancer therapy. It is most active as an iron complex. A detailed spectroscopic and theoretical study of the ferric form of the drug, Fe(III)BLM, and its activated form, ABLM, is reported. ABLM, which has been shown to be a ferric hydroperoxide complex, is the last detectable intermediate in the reaction cycle of BLM that leads to a DNA radical and subsequent cleavage. Both forms of the drug are low-spin Fe(III) complexes and were studied with electron paramagnetic resonance (EPR), magnetic circular dichroism (MCD), and absorption (ABS) spectroscopy. In addition, resonance Raman (rR) and circular dichroism (CD) spectra are reported for Fe(III)BLM. The *g* matrix was analyzed in detail, and Griffith's model for low-spin *d*<sup>5</sup> complexes was experimentally evaluated. A ligand field analysis of the *d*–*d* region of the optical spectra resulted in a complete determination of the ligand field parameters for both forms of the drug. Analysis of the optical and rR data led to assignment of the main ABS band at 386 nm in both Fe(III)BLM and ABLM as deprotonated amide-to-iron ligand-to-metal charge-transfer (LMCT) transitions. Revised vibrational assignments are proposed on the basis of B3LYP frequency calculations on models of Fe(III)BLM. On the basis of energetically optimized geometric models for Fe(III)BLM and ABLM the electronic structures of both forms were analyzed using density functional theory (DFT), ab initio Hartree–Fock, and INDO/S methods. Conjugation of the deprotonated amide and pyrimidine functionalities is not proposed to be a major factor in the BLM electronic structure. In agreement with experimental data the calculations show that the ligand fields of both Fe(III)BLM and ABLM are dominated by the deprotonated amide that also determines the orientation of the *t*<sub>2g</sub> hole, the orientation of the *g* matrix and Mössbauer quadrupole tensor. The main LMCT band was shown to be an amide  $\pi$ -LMCT band. The calculations were extended to study the reactivity of the drug toward DNA. The possibilities of (a) heterolytic cleavage of the O–O bond in ABLM to give Fe(V)BLM=O and H<sub>2</sub>O, (b) homolytic cleavage to give Fe(IV)BLM=O and OH•, and (c) direct attack of the hydroperoxide of ABLM on DNA to give Fe(IV)BLM=O, water, and a DNA radical were evaluated. Importantly, heterolytic cleavage is strongly suggested to be energetically unfavorable because it leads to a product which is best described as [Fe(IV)=O BLM•] with a high-energy hole localized on the deprotonated amide. Initial homolytic cleavage is also discarded on the basis of the specificity of the reaction; this leads to the new working hypothesis that ABLM chemistry proceeds by direct attack of the substrate C–H bond by the low-spin ferric hydroperoxide complex ABLM. The electronic structure contributions to such a reaction are discussed, and the relationship of ABLM and cytochrome P450 is addressed.

## 1. Introduction

Bleomycin (BLM) is a glycopeptide antibiotic produced by the fungus *Streptomyces verticillus* that is used clinically for anticancer therapy for head and neck cancer, certain lymphomas, and testicular cancer.<sup>1–3</sup> The cytotoxic activity of the drug is believed to relate to its ability to cleave double-stranded DNA selectively in the presence of reduced metal ions and dioxygen.<sup>4–6</sup>

The highest activity is found if iron is bound to the drug,<sup>7</sup> and therefore most research efforts are focused on the elucidation of the mechanism of action of this derivative.

BLM provides six endogenous ligands (Scheme 1) that can coordinate to the metal ion.<sup>4–6</sup> Unfortunately, there is no high-resolution crystal structure, and therefore current insight into the structure of FeBLM is based on chemical and spectroscopic studies as well as structural studies on other metallobleomycins.<sup>6,8–12</sup> The consensus structural features derived from these studies are: the  $\beta$ -hydroxyhistidine, pyrimidine, depro-

\* To whom correspondence should be addressed.

<sup>†</sup> Present address: Mathematisch Naturwissenschaftliche Sektion, Fachbereich für Biologie, Universität Konstanz, D-78457 Konstanz, Germany.

(1) Sikic, B. I.; Rosenzweig, M.; Carter, S. K. *Bleomycin Chemotherapy*; Academic Press: Orlando, 1985.

(2) Lazo, J. S.; Chabner, B. A. In *Cancer Chemotherapy and Biotherapy: Principles and Practice*; Chabner, B. A., Longo, D. L., Eds.; Lippincott-Raven: Philadelphia, PA, 1996; pp 379ff.

(3) Umezawa, H. in: *Anticancer Agents based on Natural Products*; Cassady, J. M., Douros, J., Eds.; Academic Press Inc., New York, 1980; pp 147ff.

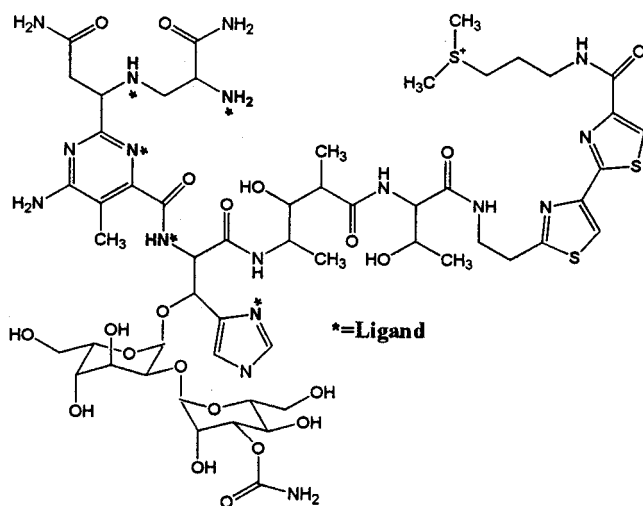
(4) Stubbe, J.; Kozarich, J. W. *Chem. Rev.* **1987**, 87, 1107.

(5) Burger, R. M. *Chem. Rev.* **1998**, 98, 1153.

(6) Stubbe, J.; Kozarich, J. W.; Wu, W.; Vanderwall, D. E. *Acc. Chem. Res.* **1996**, 29, 322.

(7) (a) Sauseville, E. A.; Peisach, J.; Horwitz, S. B. *Biochem. Biophys. Res. Commun.* **1976**, 73, 814. (b) Lown, J. W.; Sim, S. K. *Biochem. Biophys. Res. Commun.* **1977**, 77, 1150. (c) Sauseville, E. A.; Stein, R. W.; Peisach, J.; Jorwitz, S. B. *Biochemistry* **1978**, 17, 2746. (d) Burger, R. M.; Berkowitz, A. R.; Peisach, J.; Horwitz, S. B. *J. Biol. Chem.* **1980**, 255, 11832. (e) Giloni, L.; Takeshita, M.; Johnson, F.; Iden, C.; Grollman, A. P. *J. Biol. Chem.* **1981**, 256, 8608. (f) McGall, G. H.; Rabow, L. E.; Ashley, G. W.; Wu, S. H.; Kozarich, J. W.; Stubbe, J. *J. Am. Chem. Soc.* **1992**, 114, 4958. (g) Absalon, M. J.; Wu, W.; Kozarich, J. W.; Stubbe, J. *Biochemistry* **1995**, 34, 2065. (h) Absalon, M. J.; Wu, W.; Kozarich, J. W.; Stubbe, J. *Biochemistry* **1995**, 34, 2076.

Scheme 1



tonated amide, and secondary amine functionalities are thought to bind in the equatorial plane, and the primary amine of the  $\beta$ -aminoalanine part of BLM is an axial ligand.<sup>13</sup> A recent study of BLM derivatives has implicated the 3-*O*-carbamoyle substituent of the mannose sugar as a possible sixth ligand to the ferrous ion.<sup>14</sup> This sixth ligand is labile and the site for azide binding.<sup>14</sup> In Fe(III)BLM the sixth position is occupied by a hydroxide as evidenced by resonance Raman (rR) spectroscopy.<sup>15</sup> A spectroscopic study of Fe(II)BLM and a synthetic analogue, Fe(II)-PMA,<sup>16</sup> has assigned the visible absorption bands as metal-to-ligand charge-transfer (MLCT) transitions.<sup>17</sup> The observation of these moderately intense transitions indicates the presence of back-bonding between Fe(II) and the pyrimidine ligand; this bond is known to have an unusually short bond length of 2.08 Å.<sup>18</sup> These features distinguish BLM from other non-heme iron sites, and it has been suggested that BLM bridges the fields of non-heme and heme iron where the latter is dominated by  $\pi$ -back-bonding.<sup>15,17</sup>

In the presence of excess DNA and absence of reducing agents the ternary complex between Fe(II), BLM, and dioxygen

is stable and called oxy-BLM. On the basis of Mössbauer data this complex is formally described as an Fe(III)-superoxide complex,<sup>19</sup> similar to the complex formed between hemoglobin and dioxygen.<sup>20</sup> The formation of oxy-BLM is reversible. If one more electron is supplied to oxy-BLM, activated BLM (ABLM) is produced. ABLM is the last form of the drug that is observed before DNA cleavage, and its time course of disappearance correlates with the production of DNA cleavage products.<sup>21</sup>

The DNA cleavage reaction has been studied in considerable detail by a number of groups, and much insight is available on the different pathways that lead to different DNA breakdown products.<sup>4,5</sup> There are two main pathways that are both initiated by a hydrogen-atom abstraction at the C4' of the DNA ribose sugar. In the oxygen-dependent pathway the C4' radical is thought to undergo addition of O<sub>2</sub> to form a peroxy radical that after one-electron reduction yields a hydroperoxide intermediate, which after a Criegee rearrangement yields DNA cleavage products in a number of subsequent steps. The other pathway of BLM activity yields as a primary product the C4'-OH species which is unstable in alkaline media and leads to a C4 ketodeoxyribose that can be detected as an intermediate in DNA breakdown.

ABLM is the first mononuclear oxygen intermediate in biological non-heme iron environments that is stable enough for detailed spectroscopic study. This fact together with its considerable biological significance makes ABLM a major research target both as a model system for other non-heme iron environments and as a research goal in itself to better understand the antitumor activity of the drug.<sup>4-6</sup> Previously, ABLM has been studied by electron paramagnetic resonance (EPR),<sup>21-23</sup> Mössbauer,<sup>19</sup> electron nuclear double resonance (ENDOR),<sup>22,24</sup> mass spectrometry<sup>25</sup> and X-ray absorption spectroscopy (XAS).<sup>18</sup> These were instrumental in establishing that the EPR detectable species at  $g = 2.27$ , 2.17, and 1.94 (ABLM) is related to DNA cleavage<sup>21</sup> and the now accepted model that this species is a low-spin Fe(III) hydroperoxide.<sup>25,22,18</sup>

Despite extensive efforts it has not yet been possible to identify unambiguously the species that is active in C4' hydrogen-atom abstraction. It has been widely assumed that FeBLM reacts via a cytochrome P450-type mechanism<sup>26-30</sup> (Scheme 2), which involves the formation of a (hydro)peroxy-Fe(III) intermediate followed by the heterolytic cleavage of the O-O bond to produce a high-valent, formally Fe(V)=O, intermediate that then reacts with DNA by hydrogen-atom abstraction.<sup>5</sup> The possibility of the peroxide level species being the reactive species has been discussed by Sam et al.<sup>25</sup> However,

(8) (a) Wu, W.; Vanderwall, D. E.; Lui, S. M.; Tang, X. J.; Turner, C. J.; Kozarich, J. W.; Stubbe, J. *J. Am. Chem. Soc.* **1996**, *118*, 1268. (b) Wu, W.; Vanderwall, D. E.; Turner, C. J.; Kozarich, J. W.; Stubbe, J. *J. Am. Chem. Soc.* **1996**, *118*, 1281. (c) Wu, W.; Vanderwall, D. E.; Stubbe, J.; Kozarich, J. W.; Turner, C. J. *J. Am. Chem. Soc.* **1994**, *116*, 10843.

(9) (a) Gamcsik, M. P.; Glickson, J. D.; Zon, G. *J. Biomol. Struct. Dyn.* **1990**, *7*, 1117. (b) Xu, R. X.; Nettesheim, D.; Otvos, J. D.; Petering, D. H. *Biochemistry* **1994**, *33*, 907. (c) Xu, R. X.; Antholine, W. E.; Petering, D. H. *J. Biol. Chem.* **1992**, *267*, 944, 950. (d) Otvos, J. D.; Antholine, W. E.; Wehrli, S.; Petering, D. H. *Biochemistry* **1996**, *35*, 1458. (e) Mao, Q.; Fulmer, P.; Li, W.; DeRose, E. F.; Petering, D. H. *J. Biol. Chem.* **1996**, *271*, 6185.

(10) (a) Manderville, R. A.; Ellena, J. F.; Hecht, S. M. *J. Am. Chem. Soc.* **1995**, *117*, 7891. (b) Manderville, R. A.; Ellena, J. F.; Hecht, S. M. *J. Am. Chem. Soc.* **1994**, *116*, 10851.

(11) Iitaka, Y.; Nakamura, H.; Nakatani, T.; Muraoka, Y.; Fujii, A.; Takita, T.; Umezawa, H. *J. Antibiot.* **1978**, *31*, 1070.

(12) Lehmann, T. E.; Serrano, M. L.; Que, L., Jr. *Biochemistry* **2000**, *39*, 3886.

(13) Akkerman, M. A. J.; Neijman, E. W. J. F.; Wijmea, S. S.; Hilbers, C. W.; Bermel, W. *J. Am. Chem. Soc.* **1982**, *104*, 38.

(14) Loeb, K. E.; Zaleski, J. M.; Hess, C. D.; Hecht, S. M.; Solomon, E. I. *J. Am. Chem. Soc.* **1998**, *120*, 1249.

(15) Takahashi, S.; Sam, J. W.; Peisach, J.; Rousseau, D. L. *J. Am. Chem. Soc.* **1994**, *116*, 4408.

(16) Guajardo, R. J.; Hudson, S. E.; Brown, S. J.; Mascharak, P. K. *J. Am. Chem. Soc.* **1993**, *115*, 7971.

(17) Loeb, K. E.; Zaleski, J. M.; Westre, T. E.; Guajardo, R. J.; Mascharak, P. K.; Hedman, B.; Hodgson, K. O.; Solomon, E. I. *J. Am. Chem. Soc.* **1995**, *117*, 4545.

(18) Westre, T. E.; Loeb, K. E.; Zaleski, J. M.; Hedman, B.; Hodgson, K. O.; Solomon, E. I. *J. Am. Chem. Soc.* **1995**, *117*, 1309.

(19) Burger, R. M.; Kent, T. A.; Horwitz, S. B.; Münck, E.; Peisach, J. *J. Biol. Chem.* **1983**, *258*, 1559.

(20) (a) Weiss, J. J. *Nature* **1964**, *96*, 83. (b) Pauling, L.; Coryell, C. D. *Proc. Natl. Acad. Sci. U.S.A.* **1936**, *22*, 210. (c) Goddard, W. A., III; Olafson, B. D. *Proc. Natl. Acad. Sci. U.S.A.* **1975**, *72*, 2335.

(21) Burger, R. M.; Peisach, J.; Horwitz, S. B. *J. Biol. Chem.* **1981**, *256*, 11636.

(22) Veselov, A.; Sun, H.; Sienkiewicz, A.; Taylor, H.; Burger, R. M.; Scholes, C. P. *J. Am. Chem. Soc.* **1995**, *117*, 7508.

(23) Sugiura, Y. *J. Am. Chem. Soc.* **1980**, *102*, 5208.

(24) Veselov, A.; Burger, R. M.; Scholes, C. P. *J. Am. Chem. Soc.* **1998**, *120*, 1030.

(25) Sam, J. W.; Tang, X.-J.; Peisach, J. *J. Am. Chem. Soc.* **1994**, *116*, 5250.

(26) Traylor, T. G.; Traylor, P. S. In *Active Oxygen in Chemistry and Biology*; Blackie Academic and Professional: New York, 1995; p 84.

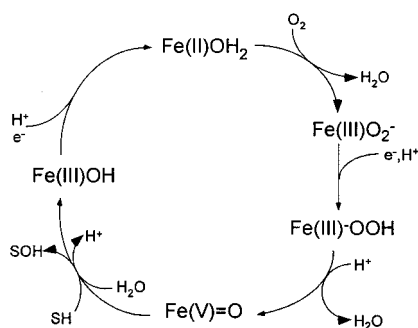
(27) Groves, J. T. *J. Chem. Educ.* **1985**, *62*, 928.

(28) Dawson, J. H. *Science* **1988**, *240*, 433.

(29) Sono, M.; Roach, M. P.; Coulter, E. D.; Dawson, J. H. *Chem. Rev.* **1996**, *96*, 2841.

(30) *Cytochrome P450: Structure, Mechanism and Biochemistry*; Ortiz-de Montellano, P. R., Ed.; Plenum: New York, 1985.

Scheme 2



the possible breakdown of this species to a short-lived iron-oxo species that does the actual chemistry could not be ruled out by their experiments.<sup>25</sup>

Several groups have carried out kinetic studies to elucidate the mechanism of DNA cleavage by BLM.<sup>4,31–37</sup> Two sets of studies are particularly relevant for the present work that focuses on the first step of BLM action, namely the abstraction of a hydrogen atom from the C4' position of the DNA ribose sugar. Burger and co-workers have studied the effect of the oxygen isotope<sup>38</sup> on the decay of ABLM,<sup>32</sup> which is known to be first order in the concentration of ABLM.<sup>21</sup> They concluded that the isotope data are most consistent with either homo- or heterolytic cleavage of the O–O bond in the rate-limiting step. Stubbe, Kozarich, and co-workers showed that labeling of the C4' position of DNA leads to a selection effect of 7.5–12.5 and suggested that carbon–hydrogen bond cleavage is the rate-limiting step in DNA cleavage.<sup>37</sup>

In this work, EPR, absorption (ABS), circular dichroism (CD), magnetic circular dichroism (MCD), and rR spectroscopies are used to investigate the geometric and electronic structure of ABLM and Fe(III)BLM, the low-spin ferric form of the drug. The analysis of the spectroscopic data provides for the first time a detailed description of the electronic structure of ABLM. Molecular orbital (MO) calculations at the gradient corrected density functional (DFT) and semiempirical INDO/S levels have been correlated to the data to obtain an experimentally calibrated bonding scheme. Calculations have then been used to extend the experimental data to obtain insight into the mechanism of action of ABLM. From these studies, the emerging hypothesis is that ABLM does not follow a cytochrome P450-type mechanism but rather that the electronic structure that exists in ABLM and potentially also other non-heme iron sites might be suitable for direct attack of the hydroperoxide on the substrate C–H bond.

## 2. Materials and Methods

**2.1. Sample Preparation.** Blenoxane (a mixture of 60% BLM A<sub>2</sub>, 30% BLM B<sub>2</sub>, and 10% other BLM congeners) was donated by Bristol Meyers Squibb and used without further purification. The differences

in the terminal amine functionality have no influence on the spectroscopic properties of the metal ion.<sup>14,39</sup> Fe(III)BLM was prepared by anaerobic addition of Fe(II)(NH<sub>4</sub>)<sub>2</sub>(SO<sub>4</sub>)<sub>2</sub>·6H<sub>2</sub>O (FeAS, Manufacturing Chemists, Inc.) in slightly less than stoichiometric amount to an apo-BLM solution consisting of equal volumes of buffer (150 mM HEPES, pH = 7.8) and glassing agent (50% glycerol). Subsequent air oxidation for at least 1 h at 4 °C yielded spectroscopically pure Fe(III)BLM. The characteristic yellow/tan color of Fe(III)BLM appears within the first few seconds of the reaction. The effects of ethylene glycol and glycerol were tested by monitoring the room-temperature (RT) CD and low-temperature (LT) MCD spectra of Fe(III)BLM. They were found to have no influence on the spectra in both the near-IR (NIR) and visible energy regions. The final concentration was dependent on the spectroscopic technique employed and ranged between 1 and 25 mM iron.

ABLM was prepared in high yield (see below) from the reaction of Fe(III)BLM with H<sub>2</sub>O<sub>2</sub> (Mallinckrodt). The alternative pathway that yields ABLM from the reaction of Fe(II)BLM and O<sub>2</sub> gives a mixture of species. For high concentration samples (~4mM), a small aliquot of H<sub>2</sub>O<sub>2</sub> (5 μL) was added to 120 μL of Fe(III)BLM, mixed for 10 s, syringed into a 3 mm EPR tube or 3 mm path length MCD cells, and frozen ~25 s after the start of the reaction. For low-concentration samples (~1–2 mM), a small aliquot of H<sub>2</sub>O<sub>2</sub> (100-fold excess) was added to 30 μL of Fe(III)BLM, mixed for 5 s, diluted with 70 μL of a buffer/ethylene glycol solution, syringed into a 3 mm EPR tube or a 1.6 mm path length MCD cell, and frozen ~25 s after the initiation of the reaction. Parallel EPR tubes were prepared with all MCD samples to allow quantitation of ABLM and resolution of additional components in the reaction mixture, namely, unreacted low-spin Fe(III)BLM, residual high-spin Fe(III)BLM, and degradation product from the decay of the intermediate.<sup>40</sup> This method was used previously in the preparation of XAS samples and proven reliable as it resulted in superimposable EPR spectra for the EPR tubes and XAS samples.<sup>18</sup>

**2.2. EPR Spectroscopy.** EPR spectra were recorded at liquid helium temperatures on a Bruker 220-D SRC spectrometer, equipped with an Air Products Helitran liquid helium cryostat. Temperatures were measured with a carbon glass resistor mounted in an EPR tube. Samples for EPR spectroscopy were ~0.5–2 mM in Fe. The presence of 1 M Na<sub>2</sub>SO<sub>4</sub> used for rR experiments did not affect the EPR spectra. EPR spectra were simulated with an updated version of the program EPR<sup>41</sup> using methods similar to those described in the literature.<sup>42</sup> EPR spectra at 77 K were also routinely measured. The concentrations of Fe(III)-BLM and ABLM were determined by spin quantitation using the software package Spectra Calc. A 1 mM CuSO<sub>4</sub>·5H<sub>2</sub>O (Mallinckrodt) solution in 2 mM HCl and 2 M NaClO<sub>4</sub> (Fisher) and a 3 mM Fe(III)-EDTA solution in 50/50 glycerol (Baker)/water were used as standards in the *g* = 2 and *g* = 4.3 regions, respectively. The Fe(III)EDTA solution was prepared by stirring Fe(III)Cl<sub>3</sub>·6H<sub>2</sub>O with excess Na<sub>2</sub>EDTA·2H<sub>2</sub>O (Aldrich) for several hours. Typically the low-spin Fe(III)BLM samples contained less than 5% of a high-spin contaminant. This method indicated that the samples ranged from 70 to 85% ABLM, 5–10% low-spin Fe(III)BLM, 5–10% high-spin Fe(III)BLM, and 0–10% degradation products.

**2.3. ABS Spectroscopy.** RT ABS spectra were recorded on HP8452A diode array and Cary 17 spectrophotometers. LT (at 14 K) ABS spectra were obtained in the double beam mode of the Cary 17 spectrophotometer using a Janis Research Super Vari-Temp liquid helium cryostat.

**2.4. CD and MCD Spectroscopy.** MCD spectra were collected on CD spectropolarimeters (Jasco 500, S1, and S20 photomultiplier tubes for the UV/vis/near-IR regions and J200, InSb detector for the near-IR

(31) Burger, R. M.; Drlica, K. in: Meunier, B., Ed.; *DNA and RNA Cleavers and Chemotherapy of Cancer and Viral Diseases*; Kluwer Academic Publishers: The Netherlands, 1996; pp 91ff.

(32) Burger, R. M.; Tian, G.; Drlica, K. *J. Am. Chem. Soc.* **1995**, *117*, 1167.

(33) Burger, R. M.; Horowitz, S. B.; Peisach, J.; Wittenberg, J. B. *J. Biol. Chem.* **1979**, *254*, 12299.

(34) Burger, R. M.; Drlica, K.; Birdsall, B. *J. Biol. Chem.* **1994**, *269*, 25978.

(35) Burger, R. M.; Projan, S. J.; Horwitz, S. B.; Peisach, J. *J. Biol. Chem.* **1986**, *261*, 15955.

(36) Worth, L., Jr.; Frank, B. L.; Christner, D. F.; Absalon, M. J.; Stubbe, J.; Kozarich, J. W. *Biochemistry* **1993**, *32*, 2601.

(37) Wu, J. C.; Kozarich, J. W. *Biochemistry* **1985**, *24*, 7562.

(38) Tian, G.; Klinman, J. P. *J. Am. Chem. Soc.* **1993**, *115*, 8891.

(39) Loeb, K. E. Spectroscopic definition of the Non-Heme Ferrous Active Sites in Bleomycin and Phenylalanine Hydroxylase: Relevance to Oxygen Activation. Ph.D. Thesis, Stanford University, 1997.

(40) The concentration of degradation products follows from the known total iron concentration and the concentrations of (a) ABLM, (b) low-spin ferric BLM and (c) high-spin ferric BLM that were individually determined through double integration of the relevant parts of the EPR spectrum.

(41) Neese, F. Quantum Chemistry Program Exchange, University of Indiana, IN. *Bulletin* **15**: 5, **1995**.

(42) Gaffney, B. J.; Silverstone, H. J. In *Biological Magnetic Resonance, Vol 13: EMR of Paramagnetic Molecules*; Berliner, J., Reuben, J., Eds.; Plenum Press: New York, 1993; pp 1–57.



region) with sample compartments modified to accommodate magnetocryostats (Oxford instruments, SM4-7T or SM4000-7T). High-quality optical glasses were obtained by adding 50% glycerol to the samples that were frozen in metallic sample compartments between two Infrasil quartz disks separated by 1.6 or 3 mm neoprene spacers. Control experiments with poly(ethylene glycol) as glassing agents showed no difference compared to the results of the glycerol experiments in either RT ABS, RT CD, or LT MCD spectra. Experiments in the near-IR (700–2000 nm) were done using deuterated buffers (99.9 atom % D; Cambridge Isotope Labs) and  $d_3$ -glycerol (98 atom % D; Aldrich). For variable-temperature variable-field (VTVH) MCD spectroscopy accurate temperatures were measured with a carbon glass resistor inserted into the sample cell.

RT CD spectra were obtained using the same instrumentation. The known contributions due to low-spin Fe(III)BLM, a small high-spin ferric component, and degradation product were subtracted from the MCD spectrum of ABLM with little change in its overall shape. Similarly, small differences in the level of purity of ABLM samples (ranging from 70 to 85%) did not greatly affect the observed spectral features, indicating that they are dominated by ABLM.

Iterative, simultaneous Gaussian fits to the LT ABS and MCD spectra were carried out using the programs Origin 4.0 (Microcal Software Inc., U.S.A.) and Peak Fit 4 (AISN Software Inc., U.S.A.).

**2.5. RR Spectroscopy.** RR spectra were obtained using a series of lines of  $\text{Kr}^+$  (Coherent 190C-K) and  $\text{Ar}^+$  (Coherent Sabre 25/7) ion lasers with incident power in the 5–30 mW range and a  $\sim 135^\circ$  backscattering geometry. The scattered light was dispersed by a triple monochromator (Spex 1877 CP, equipped with 1200, 1800, and 2400 groves/mm gratings) and detected with a back-illuminated CCD detector (Princeton instruments ST-135). Raman data were obtained for both liquid and frozen solution samples using NMR tubes. In the latter case a liquid nitrogen flow system was used to cool the samples to  $\sim 170$  K. Data at liquid nitrogen temperatures were obtained using an EPR dewar. Raman intensities were calibrated using 1 M  $\text{Na}_2\text{SO}_4$  as an internal standard.  $\text{Na}_2\text{SO}_4$  was found to have no effect on the EPR spectra of Fe(III)BLM. Raman shifts were calibrated using the Raman peaks of propionitrile as a standard. Depending on the excitation wavelength, sample concentrations ranged from  $\sim 1$  mM at higher energies ( $< 400$  nm) to  $\sim 25$  mM at lower energies ( $> 400$ – $500$  nm) to minimize self-absorption effects.

**2.6. Density Functional Calculations.** Calculations were performed on an IBM 3BT-RS/6000 workstation using the Amsterdam density functional (ADF) program version 2.0.1.<sup>43</sup> The local exchange-correlation approximation (LDA) of Vosko, Wilk, and Nusair<sup>44</sup> was used together with the gradient corrections of Becke<sup>45</sup> for the exchange and Perdew<sup>46</sup> for the correlation. All calculations were of the spin-polarized type. An uncontracted triple- $\zeta$  basis set (ADF basis set IV) with a single polarization function was used for all atoms. The iron basis was further enhanced with an  $f$  polarization function of exponent 1.5. Core orbitals were frozen through 1s (N,O), 2p (S), and 3p (Fe). Several calculations were also carried out with the more economical ADF basis set II with similar results for relative energies.

Spin-unrestricted B3LYP<sup>47</sup> and HF calculations were carried out with the Gaussian 94 program suite.<sup>48</sup> A variety of basis sets were employed. The DGAUSS DZVP basis set<sup>49</sup> obtained from the EMSL library<sup>50</sup>

proved to be computationally efficient and showed excellent convergence properties. Typically SCF convergence for low-spin ferric species is problematic but could usually be achieved by first carrying out a UHF calculation with the DGAUSS DZVP basis followed by a B3LYP calculation with the target basis set (unless otherwise noted 6-31G\*\* for the ligands and 6-311G\*\* for the metal) and a level shift of 0.1 hartree (Eh). Natural populations analysis employed the method of Weinhold and co-workers.<sup>51</sup>

Gaussian 94 was also used for B3LYP level geometry optimizations and frequency calculations on substrate species. For the smaller ligand species the 6-311++G\*\* basis set was used. The larger model [(pyrimidine)(amide)(Ga)]<sup>−</sup> was treated with the 6-311G basis.

In estimating reaction energies, zero-point effects have been neglected throughout. Due to the large number and size of the molecules studied and computational limitations, full geometry optimization at the same level of theory was not feasible, and semiempirical (see below) and molecular mechanics (MM3 force field as implemented in the CAChe software<sup>52</sup>) geometries were employed. This together with the inherent uncertainties in the functionals employed limits the accuracy of the numbers that were obtained to  $\sim 10$ – $20$  kcal/mol. This should be a conservative estimate; for the test case where comparison with the literature was feasible, that is, the reaction of peroxy-cytochrome P450 to compound I, the error introduced by the semiempirical geometries was less than 5 kcal/mol. Nevertheless, we do not rely on small differences in the calculated numbers. In the cases considered below the differences in reaction energies larger than 20 kcal/mol are taken to be meaningful.

**2.7. Semiempirical Calculations.** All semiempirical calculations reported were of the valence-only type and carried out with the program Orca developed by FN.<sup>53</sup> The INDO/S model of Zerner and co-workers<sup>54</sup> was used together with the valence shell ionization potentials and Slater–Condon parameters listed by Bacon and Zerner<sup>54b</sup> and the standard interaction factors  $f_{p,p\sigma} = 1.266$  and  $f_{p,p\pi} = 0.585$ . No change of semiempirical parameters was found necessary for the present study. In most cases restricted open shell (ROHF)<sup>55,56</sup> self-consistent field (SCF) calculations were used. To provide orbitals suitable for subsequent multireference configuration interaction (MR-CI) studies the spin-averaged Hartree–Fock (SAHF) method<sup>57</sup> proved to be useful.

In the case of low-spin ferric species, five electrons in three orbitals made up the active space. This level of theory is denoted SAHF(5,3). This procedure yields a clear distinction between iron  $t_{2g}$ -like orbitals and ligand orbitals that is not apparent in standard ROHF calculations and also shows much stronger convergence because it includes all three low-lying ( $< 5000$   $\text{cm}^{-1}$ ) excited doublet states. The CI matrix was formed using a Rumer diagram algorithm.<sup>58</sup> The construction of a suitable excitation scheme is, however, not trivial. The use of three

(49) Godbout, N.; Salahub, D. R.; Andzelm, J.; Wimmer, E. *Can. J. Chem.* **1992**, *70*, 560.

(50) Basis sets were obtained from the Extensible Computational Chemistry Environment Basis Set Database, Version Mon Apr 17 10:05:30 PDT 2000, as developed and distributed by the Molecular Science Computing Facility, Environmental and Molecular Sciences Laboratory which is part of the Pacific Northwest Laboratory, P.O. Box 999, Richland, WA 99352, and funded by the U.S. Department of Energy. The Pacific Northwest Laboratory is a multiprogram laboratory operated by Battelle Memorial Institute for the U.S. Department of Energy under contract DE-AC06-76RLO 1830. Contact David Feller or Karen Schuchardt for further information. <http://www.emsl.pnl.gov:2080/forms/basisform.html>.

(51) Glendening, E. D.; Reed, A. E.; Carpenter, J. E.; Weinhold, F. *NBO*, version 3.1, distributed with Gaussian94.

(52) Quantum CAChe, Version 3.2, Oxford Molecular Ltd, 1999.

(53) Neese, F.; Orca: an ab initio and semiempirical LCAO SCF-MO/MRCI package, version 1.0, unpublished.

(54) (a) Ridley, J.; Zerner, M. C. *Theor. Chim. Acta* **1973**, *32*, 111. (b) Bacon, A. D.; Zerner, M. C. *Theor. Chim. Acta* **1979**, *53*, 21. (c) Zerner, M. C.; Loew, G. H.; Kirchner, R. F.; Mueller-Westerhoff, U. T. *J. Am. Chem. Soc.* **1980**, *102*, 589. (d) Anderson, W. P.; Edwards, W. D.; Zerner, M. C. *Inorg. Chem.* **1986**, *25*, 2728.

(55) Edwards, W. D.; Zerner, M. C. *Theor. Chim. Acta* **1987**, *72*, 347.

(56) (a) Fernandez-Rico, J.; de la Vega, J. M. G.; Fernandez-Alonso, J. I. *J. Comput. Chem.* **1983**, *4*, 33. (b) Fernandez-Rico, J.; Paniagua, M.; Fernandez-Alonso, J. I.; Fantucci, P. J. *Comput. Chem.* **1983**, *4*, 41.

(57) (a) Stavrev, K. K.; Zerner, M. C. *Int. J. Quantum Chem.* **1997**, *65*, 877. (b) Zerner, M. C. *Int. J. Quantum Chem.* **1989**, XXXV, 567.

(43) (a) Baerends, E. J.; Ellis, D. E.; Ros, P. *J. Chem. Phys.* **1973**, *2*, 42. (b) te Velde, G.; Baerends, E. J. *J. Comput. Phys.* **1992**, *99*, 84.

(44) Vosko, S. H.; Wilk, L.; Nusair, M. *Can. J. Phys.* **1980**, *58*, 1200.

(45) Becke, A. D. *J. Chem. Phys.* **1986**, *84*, 4524.

(46) Perdew, J. P.; Chevary, J. A.; Vosko, S. H.; Jackson, K. A.; Pederson, M. R.; Singh, D. J.; Fiolhais, C. *Phys. Rev. A* **1992**, *46*, 6671.

(47) (a) Becke, A. D. *Phys. Rev. A* **1988**, *38*, 3098. (b) Becke, A. D. *J. Chem. Phys.* **1993**, *98*, 1372. (c) Becke, A. D. *J. Chem. Phys.* **1993**, *98*, 5648.

(48) Frisch, M. J.; Trucks, G. W.; Schlegel, H. B.; Gill, P. M. W.; Johnson, B. G.; Robb, M. A.; Cheeseman, J. R.; Keith, T.; Petersson, G. A.; Montgomery, J. A.; Raghavachari, K.; Al-Laham, M. A.; Zakrzewski, V. G.; Ortiz, J. V.; Foresman, J. B.; Cioslowski, J.; Stefanov, B. B.; Nanayakkara, A.; Challacombe, M.; Peng, C. Y.; Ayala, P. Y.; Chen, W.; Wong, M. W.; Andres, J. L.; Replogle, E. S.; Gomperts, R.; Martin, R. L.; Fox, D. J.; Binkley, J. S.; Defrees, D. J.; Baker, J.; Stewart, J. P.; Head-Gordon, M.; Gonzalez, C.; Pople, J. A. *Gaussian 94*, revision C.3; Gaussian, Inc.: Pittsburgh, PA, 1995.

references (the three components of the low-symmetry split  ${}^2T_{2g}$  ground state) includes at the MR-CIS level (MR-CI with single excitations relative to the reference configurations) important double excitations that tend to more strongly stabilize the ground state but not the excited states. Consequently, transition energies are usually overestimated at this level. The scheme that was finally used employed a single reference together with all single excitations within a suitable orbital window and all double excitations within the iron d-set and from the highest ligand orbitals into the d-orbitals. All configurations state functions (CSFs) with zeroth order energy within  $50\,000\text{ cm}^{-1}$  from the zeroth-order ground state were included in the “selection set”, and all CSFs with an interaction energy of  $\geq 50\text{ cm}^{-1}$  with any of the selection set CSFs were included in the variational calculation. The energetic effects of the “weakly interacting” remaining CSFs were treated by second-order Epstein–Nesbet perturbation theory.

For the high-valent iron–oxo species, it was found that a suitable active space in SAHF consists of nine electrons in six orbitals (SAHF(9,6)). These include the three iron  $t_{2g}$ -like orbitals, the oxo  $p_x$  and  $p_y$  orbitals, and a ligand orbital. A full CI (CAS) within this active space then gives a useful approximation to the ground-state wave function that is conveniently analyzed through the natural orbitals (NOs<sup>59</sup>) of this wave function.

Since the CI calculations led to very strong mixing of individual CSFs, it proved helpful to analyze the NOs of individual excited states. Either the NOs of the excited state or NOs that were obtained from the average of the ground state and the excited-state density were considered. In the latter case the acceptor NO has an occupation of  $\sim 0.5$  and the donor of  $\sim 1.5$  or  $\sim 0.5$ , depending on whether it was singly or doubly occupied in the ground state.

Transition intensities were computed from the CI wave functions in the dipole length formalism with only one center terms retained. The  $g$ -matrix was computed directly from the CI wave functions by a recently described formalism.<sup>60</sup> The iron quadrupole tensor was also computed from the density matrix obtained from the CI calculations. In the valence-only framework the field gradient tensor is computed from the following expressions:<sup>61</sup>

$$V_{ab} = -(1 - R_S)\text{trace}(\mathbf{P}\mathbf{v}^{ab}) + (1 - R_\infty)\sum_{B \neq \text{Fe}} Q_B R_B^{-5} \{3\mathbf{R}_a \mathbf{R}_b - R^2\} \quad (1)$$

$$\mathbf{v}_{ij}^{ab} = \left\langle \phi_i \left| \frac{\partial}{\partial \mathbf{r}_a^{\text{Fe}}} \frac{\partial}{\partial \mathbf{r}_b^{\text{Fe}}} \frac{1}{r_{\text{Fe}}} \right| \phi_j \right\rangle \quad (2)$$

$$\Delta E_Q = \frac{1}{2} e^2 V_{\text{max}} Q \sqrt{1 + \frac{1}{3} \eta^2} \quad (3)$$

$$\eta = (V_{\text{min}} - V_{\text{mid}})/V_{\text{max}} \quad (4)$$

The first term in eq 1 represents the “direct electronic contribution” to the field gradient due to the electron distribution at the central iron, and the second term is the “lattice contribution” which is due to the net charges of the surrounding atoms. Here  $a, b = x, y, z$ ,  $\mathbf{P}$  is the first-order density matrix,  $Q_B$  is the charge of atom B,  $\mathbf{R}_B$  is the vector from atom B to the central iron and  $\mathbf{r}_{\text{Fe}}^{\text{Fe}}$  is the electron position relative to the central iron.  $\phi_i$  and  $\phi_j$  are basis functions localized on the central iron. The neglect of multicenter contributions is reasonable due to the  $r^{-3}$  dependence of the field gradient operator. For the one center matrix element of  $\langle \mathbf{r}_{\text{Fe}}^{-3} \rangle$  the value  $4.861\text{ au}^{-3}$  was taken from relativistic atomic calculations<sup>62</sup> for the d-electrons and  $1.620\text{ au}^{-3}$  for the

p-electrons.  $V_{\text{max}}$  is the numerically largest eigenvalue of the  $\mathbf{V}$  matrix,  $V_{\text{min}}$ , the smallest, and  $V_{\text{mid}}$ , the intermediate element.  $Q$  is the quadrupole moment of the iron nucleus and was taken as 0.15 barn. The Sternheimer antishielding factors  $(1 - R_S)$  and  $(1 - R_\infty)$  compensate for aspherical distortions of the core electron densities that are not present in valence-only calculations and were set to 0.92 and 10.5 respectively.<sup>63</sup> Finally,  $\Delta E_Q$  is the quadrupole splitting measured by Mössbauer spectroscopy, and  $\eta$  is the asymmetry parameter. No attempt has been made to change any of the empirical parameters entering eqs 1–4 to improve the agreement between the experimental and calculated numbers.

Geometry optimizations were of the analytic gradient-driven type<sup>64</sup> and were carried out in Cartesian coordinates using the NDDO/1 Hamiltonian.<sup>65</sup> NDDO/1 is similar to the INDO/1 method of Zerner and co-workers<sup>66</sup> but includes more anisotropy in the important Coulomb electron–electron repulsion integrals. Two center Coulomb integrals were directly evaluated<sup>67</sup> using the contracted double- $\zeta$  STOs of Clementi and Roetti<sup>68</sup> for the iron 3d shell and standard single- $\zeta$  STOs for all other orbitals.<sup>69</sup> The iron  $\beta_0$  parameters were chosen to be  $\beta_0^d = -33\text{ eV}$  and  $\beta_0^{\text{sp}} = -2.5\text{ eV}$  on the basis of preliminary studies on a variety of iron complexes. From experience gained on  $\sim 15$  molecules, NDDO/1 is only slightly slower but more reliable than INDO/1 for metal–ligand bond distances<sup>65</sup> as well as somewhat more successful in the reproduction of geometries and rotational barriers, which was also found by others.<sup>70</sup> The formally Fe(V)=O complexes were optimized at the SAHF(9,6) level with  $S = 3/2$  and a fixed Fe=O bond length of  $1.7\text{ \AA}$ . All other optimizations were done at the ROHF level without constraints.

**2.8. Ab Initio Hartree–Fock Calculations.** Ab initio Hartree–Fock calculations with second-order Möller–Plesset correlation correction<sup>71</sup> were carried out with the PC version of the Gamess program<sup>72,73</sup> and the Stevens–Basch–Krauss effective core potential and the associated basis set (SBK,<sup>74</sup>).

The  $[\text{Fe}(\text{NH}_3)_5(\text{OOH})]^{2+}$  models used in these calculations were constructed using standard geometrical parameters. For the  $S = 5/2$  state the Fe–N bond length was set to  $2.15\text{ \AA}$ , the Fe–O bond length to  $1.90\text{ \AA}$ , and the Fe–O–OH angle was  $113^\circ$ . All of these values are consistent with previous DFT-based geometry optimizations on similar complexes. In the  $S = 1/2$  species the Fe–N bond length was set to  $2.0\text{ \AA}$ .

### 3. Results and Analysis

**3.1. Spectroscopic Data. 3.1.1. Fe(III)BLM. EPR.** EPR spectra for both Fe(III)BLM and ABLM were identical to those reported in the literature<sup>21–23</sup> in overall shape and resonance positions determined by spectral simulations for a low-spin

(62) Desclaux, J. P. *At. Nucl. Data Tables* **1973**, 12, 311.

(63) Kuramochi, H.; Noodleman, L.; Case, D. A. *J. Am. Chem. Soc.* **1997**, 119, 11442.

(64) Head, J. D.; Zerner, M. C. *Adv. Quantum Chem.* **1989**, 20, 239.

(65) Neese, F. unpublished.

(66) Zerner, M. C. ZINDO: a semiempirical program package, University of Florida, Gainesville, FL 32611.

(67) (a) Harris, F. E.; Michels, H. H. *Adv. Chem. Phys.* **1967**, 205. (b) Todd, H. D.; Kay, K. G.; Silverstone, H. J. *J. Chem. Phys.* **1970**, 53, 3951.

(68) Clementi, E.; Roetti, C. *At. Nucl. Data Tables* **1974**, 14, 177.

(69) Atkins, P. W. *Methods of Molecular Quantum Mechanics*, 2nd ed.; Oxford University Press: New York, 1983.

(70) Neeke, C.; Reinhold, J. *Theor. Chim. Acta* **1984**, 65, 99.

(71) (a) Knowles, P. J.; Andrews, J. S.; Amos, R. D.; Handy, N. C.; Pople, J. A. *Chem. Phys. Lett.* **1991**, 186, 130. (b) Lauderdale, W. J.; Stanton, J. F.; Gauss, J.; Watts, J. D.; Bartlett, R. J. *Chem. Phys. Lett.* **1991**, 187, 21.

(72) Schmidt, M. W.; Baldridge, K. K.; Boatz, J. A.; Elbert, S. T.; Gordon, M. S.; Jensen, J. J.; Koseki, S.; Matsunaga, N.; Nguyen, K. A.; Su, S.; Windus, T. L.; Dupuis, M.; Montgomery, J. A. *J. Comput. Chem.* **1993**, 14, 1347.

(73) Granovsky, A. A. *PC GAMESS*, ver. 5.2, build number 1610, Laboratory of Chemical Cybernetics: Moscow State University, Moscow, Russia, 1999. Obtained from <http://classic.chem.msu.su/gran/gameess/index.html>.

(74) (a) Stevens, W. J.; Basch, H.; Krauss M. *J. Chem. Phys.* **1984**, 81, 6026. (b) Stevens, W. J.; Basch, H.; Krauss, M.; Jasien P. *Can. J. Chem.* **1992**, 70, 612. (c) Cundari, T. R.; Stevens, W. J. *J. Chem. Phys.* **1993**, 98, 5555.

(58) (a) Boys, S. F.; Reeves, C. M.; Shavitt, I. *Nature* **1956**, 178, 1207. (b) Sutcliffe, B. T.; *J. Chem. Phys.* **1966**, 42: 1, 235. (c) Cooper, I. L.; McWeeny, R. *ibid.*, 226. (d) Reeves, C. M. *Commun. ACM* **1966**, 9: 4, 276. (e) Pauncz, R. *Spin Eigenfunctions. Construction and Use*; Plenum Press: New York and London, 1979.

(59) Shavitt, I. In *Methods of Electronic Structure Theory*; Schaefer, H. F., III, Ed.; Plenum Press: New York, 1977; pp 189ff.

(60) Neese, F.; Solomon, E. I. *Inorg. Chem.* **1998**, 37, 6568.

(61) (a) Gülich, P.; Link, R.; Trautwein, A. *Mössbauer Spectroscopy and Transition Metal Chemistry*; Springer: Berlin, Heidelberg, New York, 1978; Chapter 6. (b) Marathe, V. R.; Trautwein, A. In *Advances in Mössbauer Spectroscopy*; Thosar, B. V., Iyengar, P. K., Srivastava, J. K., Bhargava, S. C., Eds.; Elsevier: New York, 1985; p 398.

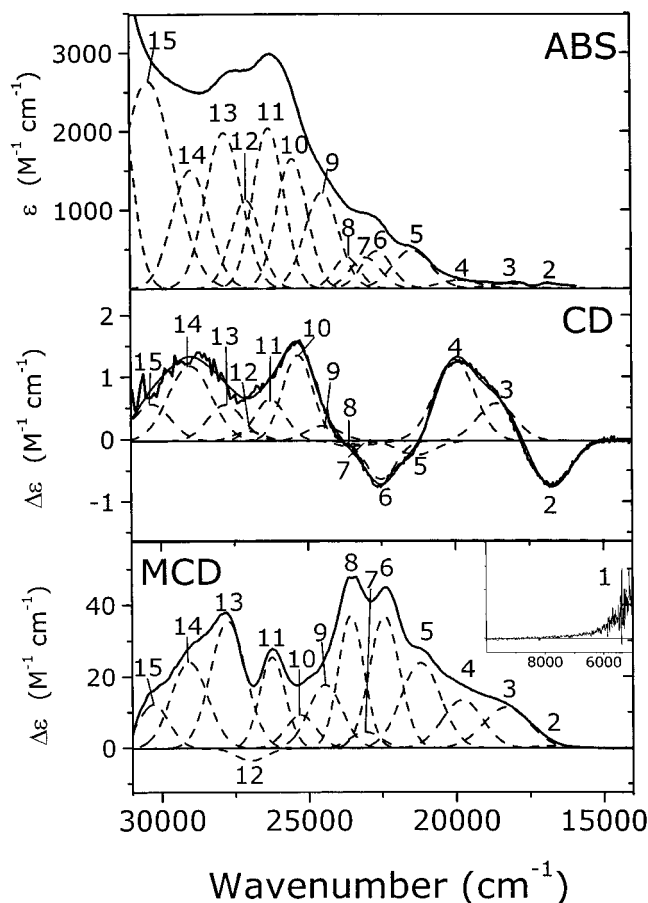


**Figure 1.** LT ABS, CD, and MCD spectra of Fe(III)BLM together with simultaneous Gaussian resolution and band numbering.

$S = 1/2$  species (Figure S1). For future reference it is noted that the  $g$ -values of Fe(III)BLM are  $g_{\max} = 2.409$ ,  $g_{\text{mid}} = 2.183$ , and  $g_{\min} = 1.890$ , whereas ABLM shows  $g_{\max} = 2.262$ ,  $g_{\text{mid}} = 2.174$ , and  $g_{\min} = 1.940$ .

**ABS/CD/MCD.** The RT ABS spectrum of Fe(III)BLM is known to be relatively featureless with a broad maximum at 386 nm ( $25\,900\text{ cm}^{-1}$ ,  $\epsilon = 3100\text{ M}^{-1}\text{ cm}^{-1}$ ) and very intense absorptions to higher energy ( $>30\,000\text{ cm}^{-1}$ ). However, a combination of LT ABS, CD, and MCD spectra revealed multiple transitions in the range  $15\,000\text{--}30\,000\text{ cm}^{-1}$  (Figure 1). The spectra were resolved with the minimum number of Gaussian bands required by the simultaneous analysis of these spectra (Figure 1, Table 1). The first detectable transition occurs below  $5000\text{ cm}^{-1}$ . The tail of this band was observed by near-IR MCD (Figure 1, MCD, inset). The exact position of the maximum is difficult to determine with high accuracy; however, a Gaussian fit to the tail gives an estimate of  $\sim 3800\text{ cm}^{-1}$ . The region between  $\sim 15\,000$  and  $\sim 6000\text{ cm}^{-1}$  contained no observable transitions (Figure 1). To higher energy intense MCD and CD transitions are observed in the region  $15\,000\text{--}25\,000\text{ cm}^{-1}$  that are associated with little ABS intensity (bands 2–8), followed by intense ABS bands (bands 9–15) that have much smaller MCD intensities based on their  $C/D$  ratios (Table 1). Interestingly, all observed MCD intensity is positive with the exception of band 12 that might have a small negative MCD intensity. Comparison to the spectra of the free ligand reveals that all of the detected transitions must be associated with the ferric ion in BLM, that is, they must be assigned to d–d and LMCT transitions. At still higher energies (beyond band 15) intense  $\pi\rightarrow\pi^*$  transitions of the pyrimidine and imidazole parts

**Table 1.** Gaussian Fit Parameters from the Analysis of Low-Temperature Optical Spectra of Fe(III)BLM<sup>a</sup>

band	$E\text{ (cm}^{-1}\text{)}$	$\text{fwhm (cm}^{-1}\text{)}$	$f_{\text{osc}}^b \times 10^4$	$R^c \times 10^4$	$C/D^d \times 10^4$
1	$\sim 3800$	–	–	–	–
2	16 740	625	2	–225	162
3	18 380	640	3	254	2860
4	19 850	670	5	200	1704
5	21 320	620	26	–7	656
6	22 510	500	21	–20	995
7	23 040	520	18	–3	1491
8	23 580	440	16	–4	1204
9	24 470	580	66	3	187
10	25 330	510	83	13	72
11	26 270	520	107	5	135
12	27 000	500	59	2	–40
13	27 790	600	129	5	228
14	29 120	560	105	15	208
15	30 290	640	265	3	37

<sup>a</sup> Energies and widths are averages from the three spectroscopic techniques. <sup>b</sup> Oscillator strength  $f_{\text{osc}} = 4.3 \times 10^{-9} \times \text{area under the absorption band}$ . <sup>c</sup> Kuhn anisotropy factor from CD spectroscopy.  $R$  = ratio of areas under the ABS and CD bands. <sup>d</sup> MCD  $C/D$  factors defined as  $C/D = (A_{\text{MCD}}/A_{\text{ABS}})(kT/\beta B)$  taken at values of  $\beta B/2kT$  where the MCD response is linear and  $A_{\text{MCD}}$  and  $A_{\text{ABS}}$  are the areas under the absorption and MCD bands from the Gaussian fitting procedure.

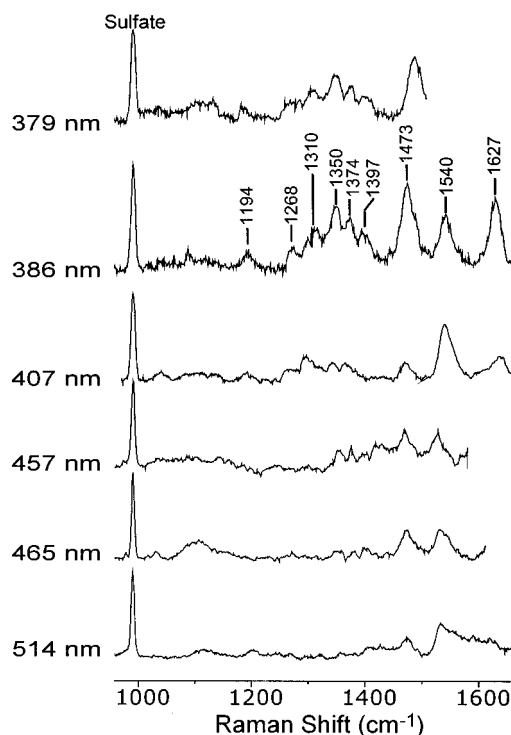


**Figure 2.** RR data obtained for Fe(III)BLM at several excitation wavelengths (indicated on the left). Peak positions are indicated on 386 nm trace.

of BLM preclude the detection of additional spectral features that could be associated with the iron/ligand interaction.

**Resonance Raman.** RR data were obtained at a series of laser lines between 379 nm ( $26\,385\text{ cm}^{-1}$ , band 11) and 514 nm ( $19\,455\text{ cm}^{-1}$ , band 4). The data in Figure 2 show two nonresonant vibrations: one at  $992\text{ cm}^{-1}$  that originates from the sulfate internal standard, and a mode at  $1540\text{ cm}^{-1}$  that was identified by Takahashi et al.<sup>15</sup> as a nonresonant vibrational mode of the bithiazole tail. Data obtained at 407 nm ( $24\,570\text{ cm}^{-1}$ ) basically agree with previously reported rR spectra,<sup>15</sup> but there are some differences in the reported wavenumbers of the vibrations. The main enhanced vibrational modes occur at 1473 and  $1627\text{ cm}^{-1}$ , together with a complex series between



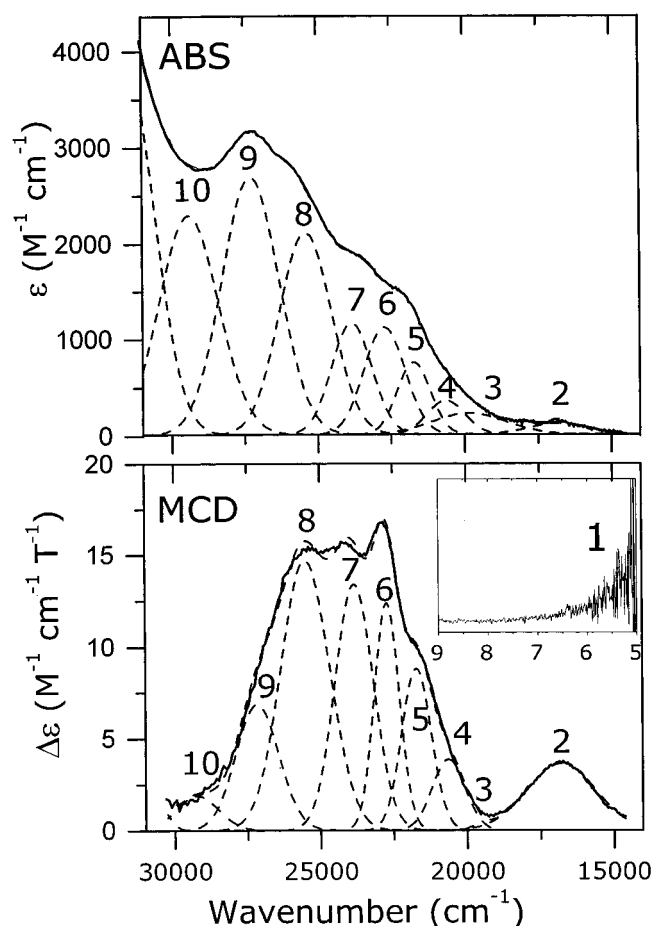


**Figure 3.** LT ABS and MCD data of ABLM together with simultaneous Gaussian resolution and band numbering.

1200 and 1400  $\text{cm}^{-1}$ . It is seen from Figure 2 that there is little resonance enhancement from bands up to 10 in the ABS and MCD spectra (514 to 407 nm lines) while there is considerable enhancement of both sets of vibrations from band 11 (386 and 379 nm lines) which is intense in ABS but weak in MCD.

**3.1.2. ABLM. ABS/MCD.** LT ABS and MCD data were also obtained for ABLM. However, due to poor glass quality LT CD spectra could not be obtained. Strikingly, there are only limited changes in both the MCD and the ABS data relative to Fe(III)BLM (Figure 3). The near-IR transition observed for Fe(III)BLM is still clearly detectable in ABLM and estimated at 3800  $\text{cm}^{-1}$  (Figure 3, MCD, inset), thus confirming the low-spin Fe(III) description of the metal center. To higher energy, ABLM shows a relatively prominent band (band 2) in the LT MCD spectra with little ABS intensity at 16 500  $\text{cm}^{-1}$  that is not present in Fe(III)BLM. The shape of this band is asymmetric, indicating that it might be associated with more than one electronic transition. The spectral envelope to higher energy is rather similar to Fe(III)BLM with a less pronounced valley in the region around 25 000  $\text{cm}^{-1}$ . As the amount of spectral information for ABLM is somewhat more limited than for Fe(III)BLM, the number of Gaussian bands used in the analysis is necessarily smaller (Figure 3 and summary in Table 2) even if more transitions may be anticipated (vide infra).

**VTVH MCD.** Since the main spectral change relative to Fe(III)BLM was observed in the region around 16 500  $\text{cm}^{-1}$  (band 2) this region was studied by VTVH MCD spectroscopy. In this region Fe(III)BLM has very little MCD intensity (Figure 1) such that there is no interference from the limited amounts of unreacted precursor that complicates the analysis

**Table 2.** Gaussian Resolution Analysis of the Low-Temperature ABS and MCD Spectra of ABLM<sup>a</sup>

band	$E$ ( $\text{cm}^{-1}$ )	fwhm ( $\text{cm}^{-1}$ )	$f_{\text{osc}} \times 10^4$	$C_0/D_0 \times 10^4$
1	~3800	-	-	-
2	16 800	2550	13	421
3	19 820	2900	32	≈0
4	20 640	1410	25	110
5	21 720	1250	46	120
6	22 730	1320	83	83
7	23 840	1350	86	132
8	25 516	2060	205	78
9	27 174	1990	278	23
10	29 234	2040	246	73

<sup>a</sup> See notes to Table 1.

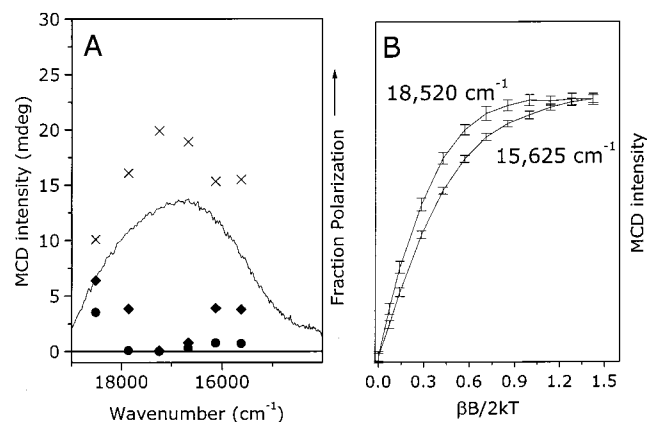


**Figure 4.** VTVH MCD data and analysis for ABLM in the region of band 2. (A) (Solid line): raw MCD data, (●): fraction  $x$ -polarized intensity ( $\parallel g_{\text{min}}$ ), (○): fraction  $y$ -polarized intensity ( $\parallel g_{\text{mid}}$ ), (×): fraction  $z$ -polarized intensity ( $\parallel g_{\text{max}}$ ). (B) Representative VTVH data taken at 1.5 and 5 K in the region of band 2 showing the differences in the data that leads to differences in the observed polarization ratios.

of the VTVH data at higher energies. The general expression for the VTVH MCD intensity of a  $S = 1/2$  system is given by:<sup>75</sup>

$$\text{MCD}(B, T) = -\frac{\gamma}{4\pi} \int_0^\pi \int_0^{2\pi} \tanh\left(\frac{g\beta B}{2kT}\right) \frac{\sin \theta}{g} \times (g_x^2 l_{xx}^2 M_{yz} + g_y^2 l_{yy}^2 M_{xz} + g_z^2 l_{zz}^2 M_{xy}) d\theta d\phi \quad (5)$$

Here the angles  $\theta$  and  $\phi$  describe the orientation of the external magnetic field relative to a molecule-fixed coordinate system,  $g_{x,y,z}$  are the principal  $g$ -values of the system,  $g = (g_x^2 l_x^2 + g_y^2 l_y^2 + g_z^2 l_z^2)^{1/2}$ ,  $l_{x,y,z}$  are direction cosines and  $\gamma$  is a collection of constants. The factors  $M_{xy,xz,yz}$  are the effective transition dipole moment products and are related to the polarization of the electronic transition under investigation.<sup>75</sup> Using the  $M$ 's as adjustable parameters, insight into the polarization of the transition can be obtained from VTVH MCD measurements on randomly oriented molecules. Under certain conditions the percentage polarization along a given  $g$  matrix direction can be estimated from:<sup>75</sup>

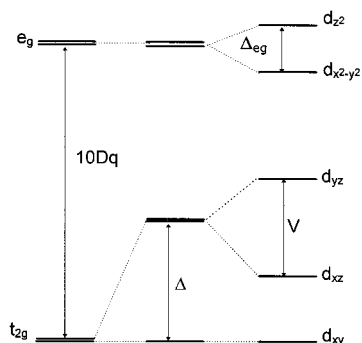
$$\%x = 100 \times \frac{(M_{xy}^{\text{eff}} M_{xz}^{\text{eff}})^2}{(M_{xy}^{\text{eff}} M_{xz}^{\text{eff}})^2 + (M_{xy}^{\text{eff}} M_{yz}^{\text{eff}})^2 + (M_{xz}^{\text{eff}} M_{yz}^{\text{eff}})^2} \quad (6)$$

and cyclic permutations of indices for the other polarization directions.

To apply eqs 5 and 6, VTVH data were taken at a number of points across band 2 as indicated in Figure 4A. Two representa-

(75) Neese, F.; Solomon, E. I. *Inorg. Chem.* **1999**, *38*, 1847.

Scheme 3



tive isotherms are shown in Figure 4B to demonstrate that the differences in polarization ratios across this band are based on significant differences in the data, indicating that more than one transition contributes in this region. Application of eqs 5 and 6 to the VTVH MCD data (Figure 4B) as a function of wavelength gives the fractional polarizations in Figure 4A. It is evident from this analysis that band 2 at the position of the maximum is mainly z-polarized, that is, along the direction of  $g_{\max}$ . This result carries electronic structure information but can only be interpreted after assigning the  $g$  matrix to a specific orientation in the molecular coordinate system as will be addressed in section 3.3.3.

**3.2. Analysis of Spectroscopic Data.** The spectral features described above together with the EPR,<sup>21–23</sup> ENDOR,<sup>22,24</sup> and Mössbauer<sup>19</sup> data reported in the literature form the basis for a comparative analysis of the electronic structures of Fe(III)BLM and ABLM. The spectra are first analyzed under the constraints of the selection rules for each spectroscopic technique<sup>76,77</sup> and then a unified picture is formulated on the basis of the data and electronic structure calculations.

On the basis of the available spectroscopic and chemical evidence, Fe(III)BLM is a six-coordinated low-spin Fe(III) complex with a distorted octahedral coordination geometry. In an octahedral crystal field the d-orbitals are split into  $t_{2g}$  and  $e_g$  sets by the parameter  $10Dq$  (Scheme 3). Lower-symmetry fields give rise to further energy splittings. An axial perturbation splits the  $e_g$  orbitals ( $d_{x^2-y^2}$  and  $d_{z^2}$ ) which can be expressed by the parameter  $\Delta_{eg}$  as well as the  $t_{2g}$  orbitals ( $d_{xz}$ ,  $d_{yz}$  and  $d_{xy}$ ) for which the axial perturbation is given by the parameter  $\Delta$ . Finally, a rhombic distortion also lifts the degeneracy of the  $d_{xz}$  and  $d_{yz}$  orbitals which is described by the parameter  $V$ . The  $(t_{2g})^5$  configuration gives rise to an orbitally triply degenerate  ${}^2T_{2g}$  ground state that splits into two components with an axial distortion and into three orbitally nondegenerate Kramers doublets when a rhombic distortion is present. By using this simple crystal field model it is possible to gain insight into the magnetic ground-state properties as well as the ligand field excited states.

**Ground State.** The orbital degeneracy of the  ${}^2T_{2g}$  ground state precludes the use of standard perturbation theory for the calculation of the  $g$  matrix.<sup>78,60</sup> In the crystal field framework, Griffith first analyzed this problem and devised a method to extract the crystal field parameters  $V$  and  $\Delta$  as a function of the  $g$ -values.<sup>79,80</sup> Griffith's method was refined by several

authors,<sup>81</sup> and there are ongoing discussions about the proper coordinate systems and co- and counter rotations of magnetic axes primarily in the field of low-spin ferric hemes.<sup>82</sup>

Here we use the Griffith–Taylor model to estimate the position of the first two ligand field states that arise from the low-symmetry splitting of the  ${}^2T_{2g}$  ground state. Since there are several mathematically possible solutions depending on the assumed signs of the  $g$ -values, it is important to have experimental constraints. In the case of Fe(III)BLM it was established by Mössbauer spectroscopy that the determinant of the  $g$ -matrix is positive.<sup>19</sup>

A more direct piece of information was obtained in this study through the observation of the near-IR MCD band around  $3800\text{ cm}^{-1}$ . We assign this band to the *second* (i.e., highest energy in Scheme 3) ligand field component of the  ${}^2T_{2g}$  state. By using a reasonable estimate of  $\zeta_{3d} \approx 380\text{ cm}^{-1}$  for the covalently reduced spin–orbit coupling constant of Fe(III), the positions of the first two ligand field bands can be predicted from Taylor's equations<sup>81c,e</sup> or a complete solution of the ligand field equations for low spin  $d^5$  systems, as we have done here. From the experimental  $g$ -values quoted in section 3.1.1 the higher-energy intra- $t_{2g}$  transition in Fe(III)BLM is predicted at  $3670\text{ cm}^{-1}$  and in ABLM at  $3950\text{ cm}^{-1}$ . Both numbers compare favorably with the estimates made from the experimental data. This is then the important constraint that allows us to conclude that all three  $g$ -values must be positive because other solutions lead to higher energies for the second ligand field band. It is seen that the energies of the ligand field transitions are 5–10 times larger than the spin–orbit coupling constant of the ferric ion. Thus, even second-order perturbation theory is a reasonable approximation, and three positive  $g$ -values are the only physically sensible solution. From perturbation theory the most important contributions are the two excitations from the doubly occupied metal-based orbitals into the singly occupied orbital. Spin–orbit coupling of the ground state to these excited states gives *positive*  $g$ -shifts ( $g_{\text{mid}}$  and  $g_{\text{max}}$ ) that can be expressed through:

$$\Delta g_{\text{max}} = \frac{2\zeta}{V} \quad (7)$$

$$\Delta g_{\text{mid}} = \frac{4\zeta}{2\Delta + V} \quad (8)$$

The much smaller *negative*  $g$ -shift ( $g_{\text{min}}$ ) is zero- to second-order. To third-order the theory of Atkins and Jamieson<sup>83</sup> gives:

$$\Delta g_{\text{min}} = -\frac{2\zeta^2}{V(2\Delta + V)} \quad (9)$$

which is of the correct sign but still too small to account for all of the  $g_{\text{min}}$ -shift that is obtained by diagonalizing the spin–orbit and ligand field matrices to all orders as done above.

There are additional contributions to the  $g$ -values that arise from LMCT excited states and more importantly from  $t_{2g} \rightarrow e_g$  excitations that will be briefly commented on below (section 3.3.3). To our knowledge this is the first direct experimental

(76) Solomon, E. I. *Comments Inorg. Chem.* **1984**, 3, 227.  
 (77) Solomon, E. I.; Hanson, M. A. In *Inorganic Electronic Spectroscopy*; Solomon, E. I., Lever, A. B. P., Eds.; Wiley & Sons: New York, 1999; Vol. II, p 1.  
 (78) Stone, A. J. *Proc. R. Soc. (London)* **1963**, A 271, 424.  
 (79) Griffith, J. S. *Nature* **1957**, 180, 30.  
 (80) Griffith, J. S. *The Theory of Transition Metal Ions*; Cambridge University Press: Cambridge, 1964.

(81) (a) Kotani, M. *Prog. Theor. Phys. Suppl.* **1961**, 17, 4. (b) Weissbluth, M. *Hemoglobin: Cooperativity and Electronic Processes*; Springer: Berlin and New York, 1973. (c) Taylor, C. P. S. *Biochim. Biophys. Acta* **1977**, 491, 137. (d) Soltis, S. M.; Strouse, C. E. *J. Am. Chem. Soc.* **1988**, 110, 2824. (e) Palmer, G. In *The Porphyrins, Part II*; Lever, A. B. P., Gray, H. B., Eds.; Addison-Wesley: London, Amsterdam, Sydney, Tokyo, 1983; p 43.  
 (82) Shokirev, N. V.; Walker, F. A. *J. Am. Chem. Soc.* **1998**, 120, 981.  
 (83) Atkins, P. W.; Jamieson, A. M. *Mol. Phys.* **1967**, 14, 425.



**Table 3.** Ligand Field Parameters for Fe(III)BLM and ABLM from the Analysis of Optical and Magnetic Data

	Fe(III)BLM	ABLM
$V$ (cm <sup>-1</sup> ) <sup>a</sup>	1880	2700
$\Delta$ (cm <sup>-1</sup> ) <sup>a</sup>	2670	2550
$10Dq$ (cm <sup>-1</sup> ) <sup>b</sup>	22 900	21 810
$\Delta_{eg}$ (cm <sup>-1</sup> ) <sup>b</sup>	2900	1370

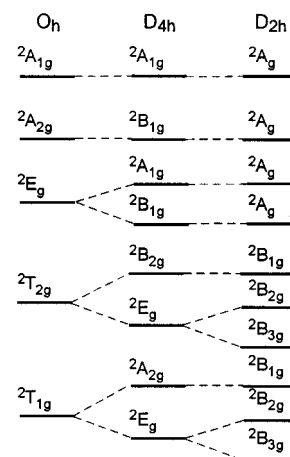
<sup>a</sup> Determined from EPR. <sup>b</sup> Determined from simultaneous analysis of ABS, CD, and MCD spectra.

test of the Griffith–Taylor model for  $^2T_{2g}$  states and shows that it is physically reasonable unlike the analogous situation for the zero-field splitting in high-spin ferric complexes, where Griffith's ligand field model has deficiencies.<sup>84,60</sup>

The values obtained for Fe(III)BLM and ABLM are collected in Table 3. While the values for  $\Delta$  are fairly similar, ABLM shows a significantly larger value of  $V$  (Scheme 3). This means that the energy difference between the highest and lowest orbital within the  $t_{2g}$  set is very similar for Fe(III)BLM and ABLM. The intermediate orbital in ABLM is energetically closer to the lowest one compared to the situation in Fe(III)BLM. This is directly reflected in the more axial EPR spectrum of ABLM. The similar value for  $\Delta$  is consistent with the near-IR MCD results that suggest a fairly similar position for the lowest-energy observed band for both Fe(III)BLM and ABLM. However, the rather small changes are interesting for the exchange of an OH<sup>-</sup> with an <sup>-</sup>OOH ligand because the orbital splittings for model low-spin Fe(III)OOH complexes are significantly larger than observed in ABLM.<sup>85</sup>

In conclusion, the ligand field parameters  $V$  and  $\Delta$  were extracted from the measured  $g$ -values. The analysis has received strong support from the experimental observation of the highest low-symmetry-split  $^2T_{2g}$  ligand field transition using near-IR MCD. It shows that ABLM has a more axial ligand field consistent with the idea to be developed in section 3.3 that the hydroperoxide is a somewhat better  $\pi$ -donor than the hydroxide ligand.

**Ligand Field versus Charge-Transfer Excited States.** The spectroscopic data lead to a clear division between d–d and LMCT states in Fe(III)BLM and ABLM through consideration of the selections rules for ABS, CD, MCD, and rR spectroscopies. First, d–d transitions have weak ABS intensities because they are Laporté forbidden.<sup>76</sup> Second, d–d transitions are magnetic dipole-allowed which gives them high CD intensities and therefore large Kuhn anisotropy factors ( $\Delta\epsilon/\epsilon$ ). Third, the transitions are metal-centered, and therefore the effective spin–orbit coupling between the ground and excited states as well as between d–d excited states is large. This gives d–d transitions high MCD intensities ( $C/D$  in Tables 1 and 2<sup>86,75</sup>). Fourth, d–d transitions lead to only minor changes in the charge density around the metal. Therefore there is very limited geometry change from the ground to the excited states, and along with the low ABS intensity, this effectively quenches the resonance enhancement of the Raman effect that is directly proportional to the displacement along each normal mode in the excited state relative to the ground state.<sup>87</sup> By applying these considerations to the spectra collected in Figures 1–3 and Tables 1 and 2, it is evident that bands 2–8 in Fe(III)BLM have all of the characteristics of d–d transitions: they are weak in ABS and strong in CD and MCD and are not

**Scheme 4**

associated with strong rR enhancements. Alternatively, bands 9–15 show all characteristics of Laporté-allowed LMCT transitions: they are strong in ABS and comparatively weak in CD and MCD, and they are also associated with strong rR enhancements. By analogy, the more limited data set for ABLM is still sufficient to conclude that there are no major changes in the interpretation of the ABS and MCD spectra and that parallel assignments apply to both cases except for band 2 in ABLM. This band has a fairly large  $C/D$  ratio which argues for d–d transitions but also has a strong  $z$ -polarization that varies over the band envelope (section 3.1.2, Figure 4) which shows that there are several electronic transitions involved. These facts together with electronic structure calculations are used in section 3.3.4 to argue that this band has contributions from both d–d and LMCT transitions.

Taken together the spectroscopic data give strong evidence that bands 1–8 in Fe(III)BLM are d–d transitions and bands 9–15 are assigned to LMCT states. The two regions can now be analyzed separately.

**Ligand Field Excited States.** Since the parameters  $V$  and  $\Delta$  have already been fixed from the  $g$ -value analysis, the two parameters in Scheme 3 that remain to be determined by the ligand field analysis are  $\Delta_{eg}$  and  $10Dq$ . The transitions from the singly occupied  $t_{2g}$  orbital into the empty  $e_g$  orbitals give rise to two excited doublet states, whereas the excitations from the doubly occupied  $t_{2g}$  orbitals lead to states with three unpaired electrons and therefore give rise to two doublet states each that only differ in the spin coupling of the unpaired electrons. Thus, there are a total of eight spin-doublet d–d excited states from this mechanism. More complexity is added by the fact that two-electron transitions, which involve the promotion of one electron from one of the doubly occupied  $t_{2g}$  orbitals into the singly occupied one plus simultaneous excitation of another electron into the  $e_g$  orbitals, are at similar energies. These doubly excited states do not carry intensity of their own, but they are energetically close to the singly excited states. Therefore, these will mix and modify their intensities and energy positions. There are a total of eight of these doubly excited ( $t_{2g}^4(e_g^1)$ ) states. Thus, if only the configurations with a single  $e_g$  electron are taken into account, there are 18 possible transitions to consider for low-spin ferric systems that potentially all contribute to the observed d–d spectrum. The terms that arise from symmetry reduction from  $O_h$  over  $D_{4h}$  to  $D_{2h}$  are shown in Scheme 4.

(84) (a) Gebhard, M. S.; Deaton, J. C.; Koch, S. A.; Millar, M.; Solomon, E. I. *J. Am. Chem. Soc.* **1990** *112*, 2217. (b) Deaton, J. C.; Gebhard, M. S.; Solomon, E. I. *Inorg. Chem.* **1989**, *28*, 877.

(85) Lehnert, N.; Ho, R.; Neese, F.; Que, L., Jr.; Solomon, E. I. Manuscript in preparation.

(86) Gerstman, B. S.; Brill, A. S. *J. Chem. Phys.* **1985**, *82*(3), 1212.

(87) (a) Lee, S. Y.; Heller, E. J. *J. Chem. Phys.* **1979**, *71*, 4777. (b) Tannor, D. J.; Heller, E. J. *J. Chem. Phys.* **1982**, *77*, 202. (c) Myers, A. B.; Mathies, R. A. In *Biological Applications of Raman Spectroscopy*; Spiro, T. G., Ed.; Wiley: New York, 1987; Vol. 2, pp 1–58. (d) Zink, J. I.; Shin, K. S. *K. Adv. Photochem.* **1991**, *16*, 119.

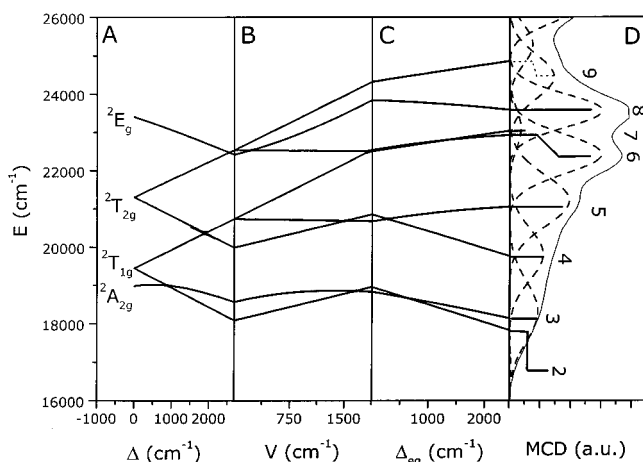


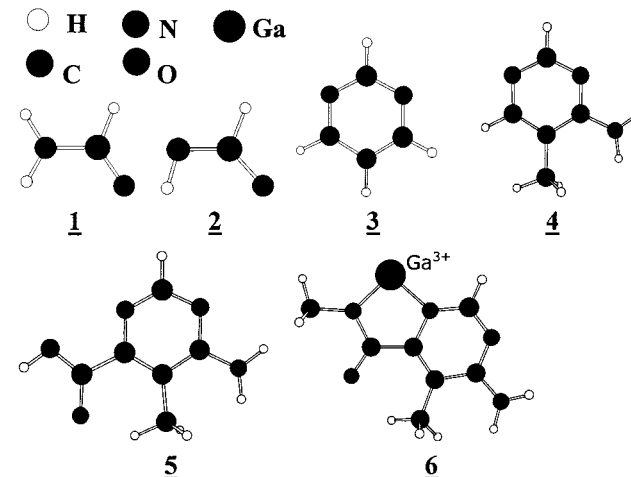
**Figure 5.** Effect of low-symmetry distortions on the band positions in Fe(III)BLM. A fixed  $10Dq$  of  $22\,660\text{ cm}^{-1}$  has been used. (A) Variation of  $\Delta$  from 0 to  $2670\text{ cm}^{-1}$  as determined from EPR spectroscopy. (B) Variation of  $V$  from 0 to  $1880\text{ cm}^{-1}$  as determined from EPR. (C) Variation of  $\Delta_{eg}$  from 0 to  $2440\text{ cm}^{-1}$ . (D) Experimental MCD with Gaussian resolution resulting from the simultaneous analysis of ABS, CD, and MCD data.  $10Dq$  and  $\Delta_{eg}$  were determined by a least-squares fit.

In the present case bands 2–8 for Fe(III)BLM and bands 3–6 for ABLM were reasonably assigned to  $t_{2g} \rightarrow e_g$  transitions (vide infra for a more detailed discussion of band 2 in ABLM). There are most certainly more d–d transitions buried under the intense LMCT envelope to higher energy. However, the observed d–d bands give enough constraints for the analysis of ligand field splittings. Given the parameters  $V$  and  $\Delta$ , the ligand-field CI matrices for  $S = 1/2$   $d^5$  systems were diagonalized, and the parameters  $10Dq$  and  $\Delta_{eg}$  were refined by a least-squares fit to the observed transition energies. In this fit a reasonable value for the Racah parameter  $B$  ( $=800\text{ cm}^{-1}$ ) has been assumed as well as the standard  $C = 4B$ .<sup>88</sup> These choices do not significantly affect the outcome of the fit. The fits appear to constrain the value of  $10Dq$  better than  $\Delta_{eg}$ , which has an uncertainty of about  $1000\text{ cm}^{-1}$ . The fit result for Fe(III)BLM is shown in Figure 5, and the best fit parameters are collected in Table 3. As can be seen from Figure 5 the number and positions of bands 2–8 are well reproduced by fitting two parameters. The errors are generally smaller than  $1000\text{ cm}^{-1}$  with the exception of band 2 which is best constrained from the CD data (Figure 1) and is calculated  $\sim 1100\text{ cm}^{-1}$  too high in energy and band 6 that is also too high in energy. The excited state close to band 9 is assigned to the first LMCT state (vide infra).

The analogous procedure for ABLM results in the parameters collected in Table 3 and Figure S2. As can be seen from this table, the changes that occur in the ligand field of ABLM relative to Fe(III)BLM are rather small. The  $10Dq$  and  $\Delta_{eg}$  values change by  $2000\text{ cm}^{-1}$  or less. This is a remarkably small change given that a hydroperoxide is expected to be a significantly stronger donor ligand than a hydroxide.

The results of the analysis also show that Fe(III)BLM has a ligand field that is relatively close to the crossover point between high- and low-spin complexes. The  $^6A_1$  state is predicted at  $\sim 3400\text{ cm}^{-1}$ . This helps to rationalize the fact that Fe(III)BLM is easily converted to the high-spin form upon lowering the pH.<sup>21</sup> It is also consistent with earlier proposals<sup>17,15</sup> that BLM bridges the fields of iron porphyrins, which are well-known for spin

**Scheme 5**



crossover, and normal non-heme iron centers that are on the high-spin side of the Tanabe–Sugano diagram.

In summary, the combined analysis of EPR, ABS, CD, MCD and rR has resulted in a description of the ligand fields of Fe(III)BLM and ABLM (Figures 5 and S2). The results demonstrate that the changes that occur in the ligand field of ABLM relative to Fe(III)BLM are rather subtle and that the hydroperoxide is a rather poor donor ligand in ABLM.

**MCD Intensity.** It is noted that for both Fe(III)BLM and ABLM all observed MCD intensity is positive. MCD intensity for a given transition  $A \rightarrow J$  has two important sources:<sup>75</sup> (a) spin–orbit coupling between the excited state  $J$  and another excited state  $K$  that necessarily induces positive MCD in one transition and negative in the other; and (b) spin–orbit coupling between the ground state,  $A$ , and an intermediate excited state,  $K$ , that can induce MCD intensity of either sign. As there is only positive MCD observed, the second mechanism is dominant in the case of Fe(III)BLM and ABLM, consistent with the large angular momentum induced by in-state spin–orbit coupling within the low-symmetry split  $^2T_{2g}$  ground term in low-spin ferric centers.

**Vibrational Assignments and Charge-Transfer Excited States.** In this section a preliminary interpretation of the Fe(III)-BLM CT region will be given on the basis of the identification of the resonance-enhanced vibrational modes observed in the Raman experiments. Specific CT assignments will be made in section 3.3.4. B3LYP/6-311G level calculations were used to estimate the harmonic vibrational frequencies and associated normal modes of several models for the pyrimidine and amide functionalities shown in Scheme 5. The focus is on the region between  $1000$  and  $1700\text{ cm}^{-1}$  in Figure 2, and the results are fully documented in the Supporting Information (Tables S1–S6). For the two cases where comparisons with experiments are feasible, namely formamide (**1**) and unsubstituted pyrimidine (**3**), the calculated vibrational frequencies agree within 3–4% with the experimental numbers. This gives confidence that the frequencies and normal modes for the other species in Scheme 5 are realistic as can also be expected from previous experience with the B3LYP method.<sup>89</sup>

Amides have a vibrational mode in the  $1630$ – $1720\text{ cm}^{-1}$  region (amide I band,<sup>90</sup>). Primary and secondary amides show an additional characteristic band around  $1550$ – $1650\text{ cm}^{-1}$  (amide II band,<sup>90</sup>) that was assigned to the  $1473\text{ cm}^{-1}$  mode in

(88) Ballhausen, C. J. *Introduction to Ligand Field Theory*; McGraw-Hill Inc.: New York, 1962.

(89) Koch, W.; Holthausen, M. C. *A Chemist's Guide to Density Functional Theory*; Wiley-VCH: Weinheim, New York, Chichester, Brisbane, Singapore, Toronto, 2000; Chapter 8 and references therein.

BLM by Takahashi et al.<sup>15</sup> However, this mode is mainly a N–H bending mode in secondary amides and a NH<sub>2</sub> scissor vibration in primary amides. Since the deprotonated amide in BLM does not have a hydrogen atom, this assignment needs to be revised. In fact, there is no characteristic amide II band in tertiary amides.<sup>90</sup> Takahashi et al. have assigned the amide II band as having primarily C–N stretching character which is in fact observed at much lower frequencies (around 1150–1250 cm<sup>−1</sup>) in both our calculations and in experiments on simple amides.<sup>90</sup>

The unsubstituted pyrimidine molecule shows 10 vibrational modes between 1000 and 1600 cm<sup>−1</sup> that belong mainly to C–N and C–C ring-stretching vibrations and C–H bends that are well reproduced by the calculations (Table S3). After the highest vibration observed at 1570 cm<sup>−1</sup> and calculated at 1578 cm<sup>−1</sup> there is a large gap, and the next vibrational mode is found above 3000 cm<sup>−1</sup>.

To gain a better understanding of the observed vibrational modes, structures **2**, **4**, **5**, and **6** in Scheme 5 were constructed as progressively better models of the pyrimidine–amide functionality of Fe(III)BLM. In the most realistic model considered (**6**) the ferric iron has been substituted by Ga<sup>3+</sup>. The first result to be noted is that deprotonation has a profound effect on the structure and vibrational properties of the amide functionality. The C=O stretching vibration moves from 1722 to 1598 cm<sup>−1</sup>, and the C–N bond length significantly shortens from 1.363 Å in **1** to 1.316 Å in **2**. In the substituted pyrimidine molecule (**4**) there are 16 vibrational modes between 1000 and 1700 cm<sup>−1</sup>. The substitution leads to limited shifts of the ring vibrations, and the additional modes are the various bending, wagging and deformation modes of the substituents (Table S4). The highest mode is calculated at 1681 cm<sup>−1</sup> and corresponds to the NH<sub>2</sub> scissor vibration. The vibrational modes of the pyrimidine-deprotonated amide construct (**5**) between 1000 and 1700 cm<sup>−1</sup> are mainly a superposition of the modes of **2** and **4** with only limited shifts relative to the individual species. Note that the important issue of electronic conjugation between the pyrimidine and deprotonated amide moieties will be addressed in section 3.3.1.

We are now in a position to analyze the vibrational modes of **6** as the most realistic model of Fe(III)BLM and thus assign the experimental rR spectrum (Figure 2, 386 nm spectrum). On the basis of the calculations there is no doubt that the vibration observed at 1627 cm<sup>−1</sup> (previously at 1611 cm<sup>−1</sup>,<sup>15</sup>) indeed belongs to the amide I band, that is, the C=O stretching vibration. This vibration is a relatively pure mode and is calculated at 1624 cm<sup>−1</sup>. It is also the only mode in this region. To higher energy there is only the NH<sub>2</sub> scissor vibration of the pyrimidine calculated at 1717 cm<sup>−1</sup>, which should not be resonance-enhanced. The strongly resonance-enhanced mode observed at 1473 cm<sup>−1</sup> is less straightforward to assign. It does not belong to the C–N stretch, which is calculated at 1185 cm<sup>−1</sup>, and we tentatively assign the vibration observed at 1194 cm<sup>−1</sup> to this mode. Alternatively, there is a C–N–C bending mode calculated at 1507 cm<sup>−1</sup> associated with the deprotonated amide moiety that is considered to be the most likely candidate for the 1473 cm<sup>−1</sup> vibrational mode in Fe(III)BLM. The region between 1200 and 1400 cm<sup>−1</sup>, which is less resonance enhanced, contains no further vibrational modes that are strongly associated with the deprotonated amide moiety. Consequently, these

**Table 4.** Assignment of the High-Frequency Vibrational Modes in Fe(III)BLM

$\nu$ (cm <sup>−1</sup> )	assignment
1627	deprotonated amide C=O stretch
1473	deprotonated amide C–N–C bend
1397	pyrimidine ring stretch
1374	pyrimidine ring stretch
1350	pyrimidine ring stretch + C–H bend
1310	pyrimidine ring stretch
1268	pyrimidine ring stretch
1194	deprotonated amide C–N stretch

remaining vibrations in this region are mainly due to pyrimidine ring stretches and aromatic C–H bends of this moiety of Fe(III)-BLM.

The vibrational assignments, which are summarized in Table 4, provide insight into the observed CT spectrum of Fe(III)BLM and thus, as discussed above, also for ABLM. The more strongly resonance-enhanced vibrations at 1627 cm<sup>−1</sup> (amide I band) and 1473 cm<sup>−1</sup> (C–N–C bend) belong to the deprotonated amide moiety, which demonstrates that the CT band responsible for resonance enhancement at 386 nm (band 11) has significant deprotonated amide-to-Fe(III) LMCT character. There is, however, also pyrimidine-to-iron LMCT character as evidenced by the less strongly resonance-enhanced pyrimidine vibrational modes in the 1200 to 1400 cm<sup>−1</sup> region in Figure 2.

**Comparison of ABLM and Fe(III)BLM.** A surprising feature of the ABLM optical spectrum is the lack of an intense hydroperoxide-to-iron LMCT band in the visible region. A number of low-spin Fe(III)OOH and Fe(III)OOR model complexes with N<sub>5</sub>OOH (or N<sub>5</sub>OOR) coordination have been prepared,<sup>91</sup> and all of them show a prominent absorption band ( $\epsilon \approx 1000\text{--}2000\text{ M}^{-1}\text{ cm}^{-1}$ ) in the visible region ( $\sim 16\,000\text{--}20\,000\text{ cm}^{-1}$ ) that has been assigned as a hydroperoxide-to-iron LMCT band from rR spectroscopy.<sup>91a</sup> The lack of this band is therefore a key feature of the ABLM electronic structure and will be explained on the basis of MO calculations in section 3.3.4. On the basis of the experimental data presented above there is no evidence to suggest that the assignment of the visible CT spectrum is substantially different for ABLM compared to that for Fe(III)BLM. The obvious exception is band 2 for ABLM that is not observed in Fe(III)BLM and was analyzed in some detail in section 3.1.2. On the basis of experimental and computational results band 2 will be assigned (section 3.3.4) to a compound band with contributions from both LMCT and ligand field transitions.

**3.3. Electronic Structure Calculations: Geometric and Electronic Structure.** **3.3.1. Electronic Structure of the Free Ligand.** As an initial step in the analysis of the electronic structure of Fe(III)BLM and ABLM it is instructive to examine the frontier orbitals of the different ligand fragments in Figure 6. The highest-lying occupied orbitals of appropriate symmetry will be most suitable for  $\sigma$ -bonding to the ferric ion and will

(90) (a) Socrates, G. *Infrared Characteristic Group Frequencies*; Wiley-Interscience: Chichester, New York, Brisbane, Toronto, 1980. (b) Dollish, F. R.; Fateley, W. G.; Benteley, F. F. *Characteristic Raman Frequencies of Organic Compounds*; Wiley-Interscience: New York, London, Sydney, Toronto, 1974.

(91) (a) Ho, R. Y. N.; Roelfes, G.; Feringa, B. L.; Que, L., Jr. *J. Am. Chem. Soc.* **1999**, *121*, 264. (b) Roelfes, G.; Lubben, M.; Chen, K.; Ho, R. Y. N.; Meetsma, A.; Genseberger, S.; Hermant, R. M.; Hage, R.; Mandal, S. K.; Young, J. V. G.; Zang, Y.; Kooijman, H.; Spek, A. L.; Que, L., Jr.; Feringa, B. L. *Inorg. Chem.* **1999**, *38*, 1929–193. (c) Zang, Y.; Elgren, T. E.; Dong, Y.; Que, L., Jr. *J. Am. Chem. Soc.* **1993**, *115*, 811. (d) Kim, J.; Larka, E.; Wilkinson, E. C.; Que, L., Jr. *Angew. Chem. Int. Ed. Engl.*, **1995**, *34*, 2048. (e) Lubben, M.; Meetsma, A.; Wilkinson, E. C.; Feringa, B.; Que, L., Jr. *Angew. Chem. Int. Ed. Engl.* **1995**, *34*, 1512. (f) Zang, Y.; Kim, J.; Dong, Y.; Wilkinson, E. C.; Appelman, E. H.; Que, L., Jr. *J. Am. Chem. Soc.* **1997**, *119*, 4197. (g) Simaan, A. J.; Banse, F.; Mialane, P.; Boussac, A.; Un, S.; Kargar-Grisel, T.; Bouchoux, G.; Girerd, J. J. *Eur. J. Inorg. Chem.* **1999**, 993. (h) Nam, W.; Ho, R.; Selverstone-Valentine, J. J. *Am. Chem. Soc.* **1991**, *113*, 7052.

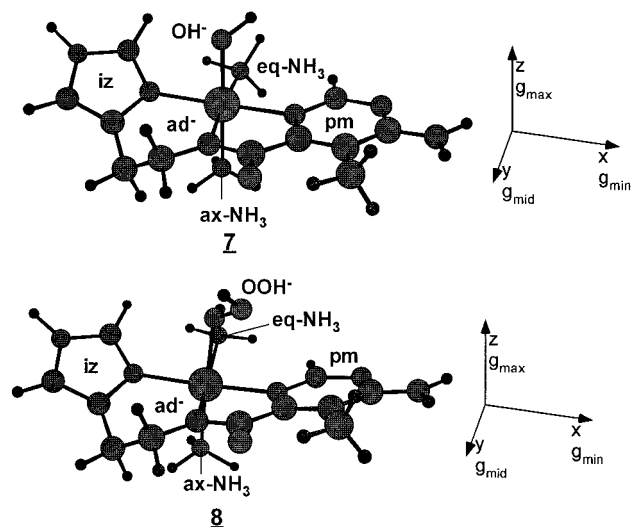




**Table 6:** Calculated Iron–Ligand Bond Distances (in Å) for Fe(III)BLM (**7**) and ABLM Models (**8**)<sup>a</sup>

	pm	iz	NH <sub>3</sub> (ax)	NH <sub>3</sub> (eq)	ad <sup>−</sup>	O(O)H <sup>−</sup>
<b>7</b>	1.994	1.971	2.006	2.003	1.922	1.870
<b>8</b>	1.986	1.965	2.011	1.997	1.925	1.972

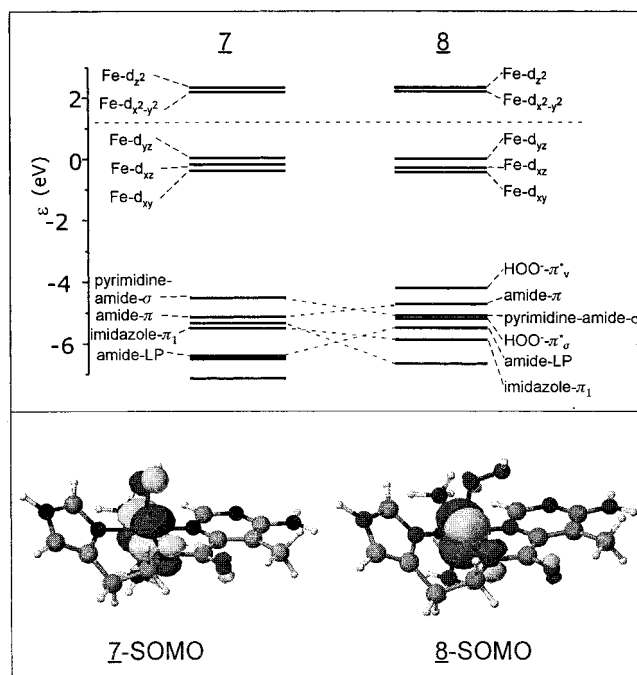
<sup>a</sup> pm = pyrimidine, iz = imidazole, ad<sup>−</sup> = deprotonated amide, NH<sub>3</sub>(ax) = axial NH<sub>3</sub>, NH<sub>3</sub>(eq) = equatorial NH<sub>3</sub>, O(O)H<sup>−</sup> = OH<sup>−</sup> for **7** and OOH<sup>−</sup> for **8**.

**Scheme 6**

The fully optimized structures are shown in Scheme 6, and the calculated metal–ligand bond distances are collected in Table 6. Both structures have a very similar overall fold with a distorted octahedral coordination geometry around the iron site. Due to the ethylene bridge between the deprotonated amide and the imidazole ligand, the imidazole ring cannot be coplanar with the pyrimidine ring. Tilt angles of 26° and 34° are obtained for **7** and **8**, respectively. For Fe(III)BLM two shells have been resolved in EXAFS experiments with distances of 2.03 and 1.90 Å,<sup>18</sup> which agree well with 2.00 and 1.90 Å from the calculations. Similarly, for ABLM two shells are observed at 2.03 and 1.89 Å,<sup>18</sup> corresponding to the calculated values of 1.99 and 1.95 Å. The agreement between calculation and experiment gives some confidence that the calculated structures are reasonably realistic.

To further probe the structure generated for ABLM several alternative geometries have been compared to the minimum-energy structure. In particular, the effects of shortening the Fe–O bond length and rotating the OOH ligand over the approximate plane spanned by the pyrimidine, deprotonated amide, and imidazole ligands have been examined, and ABS spectra were calculated for all of the structures (Supporting Information, Figures S3–S7). The calculated spectra are very sensitive to the orientation of the peroxide ligand. It is concluded from the calculations that the only structure that gives at least qualitative agreement with the experimental spectrum (Figure 3) is the minimum-energy structure **8** in Scheme 6. In this structure the projection of the peroxide O–O bond onto the equatorial plane bisects the pyrimidine and deprotonated amide ligands. The Fe–O–O bond angle is close to 120°, and the Fe–O bond is relatively long (1.972 Å) compared to ~1.90 Å obtained for other low-spin [Fe(OOH)(N<sub>5</sub>)]<sup>+</sup> complexes at the same level of theory.

**3.3.3. Electronic Ground State.** After reasonable geometric structures are obtained, the corresponding electronic structures can now be analyzed. Spectral parameters calculated from the

**Figure 7.** Molecular orbital scheme for (A) Fe(III)BLM and (B) ABLM derived from INDO/S-CI calculations.

associated wave functions can be compared to experimental data in order to gain further confidence in the resulting electronic structure description.

The results of this section are based on the INDO/S calculations (vide supra); however, the conclusions do not depend critically on this choice. Entirely consistent results with respect to the nature of the singly occupied MO (SOMO) and its covalency were obtained for the same molecules at the Hartree–Fock and B3LYP levels. As the INDO/S method is most easily applied to the calculation of spectroscopic properties our presentation is based on the results of this method.

**Fe(III)BLM.** The main feature that determines the properties of the electronic ground state of distorted octahedral low-spin ferric complexes is the nature of the SOMO. Since the SOMO derives from the  $t_{2g}$  set of iron d-orbitals, the highest MO within the  $t_{2g}$  set is determined by the  $\pi$ -bonding character of the ligands with  $\pi$ -bases destabilizing the iron d-orbitals and  $\pi$ -acids stabilizing them.

The calculated MO scheme of Fe(III)BLM (**7**) and a surface plot of the SOMO are shown in Figure 7, left, and are consistent with the general expectations for a distorted octahedral ferric complex.<sup>94</sup> The five highest MOs are mainly iron in character and correspond to the  $t_{2g}$  and  $e_g$  sets in octahedral symmetry (Table 7). The two highest MOs are based on the iron  $d_{x^2-y^2}$  and  $d_{z^2}$  orbitals and are unoccupied and  $\sigma$ -antibonding with the ligands. The highest MO within the  $t_{2g}$  set is the SOMO and is based on the iron  $d_{yz}$  orbital in a coordinate system

(94) The orbital schemes are based on CI energies in the virtual orbital approximation (VOA) with the SOMO taken as the reference orbital. The “orbital energy difference” is defined from the zeroth-order transition energy for the transition  $k \rightarrow \text{SOMO}$  for the doubly occupied MO  $k$  and from the transition  $\text{SOMO} \rightarrow a$  for a virtual orbital  $a$ . For ease of comparison the reference orbital energy for **7** and **8** were set to zero in Figure 7. This procedure is convenient because it has a close connection to the intuitive ligand field picture and also yields orbital energy differences which are closely connected to transition energies, at least for many of the more important transitions. The orbital energies obtained directly from the ROHF (or SAHF) calculation are of more limited utility because of the inapplicability of Koopman’s theorem and the importance of electronic relaxation effects in transition metal complexes.

**Table 7.** Composition of the Iron 3d-based MOs in Fe(III)BLM (7) and Wiberg Bond Orders for Iron–Ligand Bonding<sup>a</sup>

MO-label	% Fe	% pm	% ad <sup>−</sup>	% iz	% OH <sup>−</sup>	% NH <sub>3</sub> (ax)	% NH <sub>3</sub> (eq)
d <sub>z</sub> <sup>2</sup>	68.4	2.4	7.8	0.3	8.4	7.6	5.1
d <sub>x<sup>2</sup>−y<sup>2</sup></sub>	64.6	12.1	6.7	11.9	1.5	0.5	2.6
d <sub>yz</sub> SOMO	93.3	0.2	3.3	0.0	2.5	0.5	0.3
d <sub>xz</sub>	97.0	0.7	0.1	0.9	0.9	0.3	0.1
d <sub>xy</sub>	97.7	0.5	0.7	0.4	0.4	0.1	0.3
W <sub>Fe–pm</sub>	W <sub>Fe–ad</sub>	W <sub>Fe–iz</sub>	W <sub>Fe–OH</sub>	W <sub>Fe–NH3ax</sub>	W <sub>Fe–NH3eq</sub>		
0.630	0.783	0.619	0.801	0.547	0.544		

<sup>a</sup> pm = pyrimidine, ad<sup>−</sup> = deprotonated amide, iz = imidazole OH<sup>−</sup> = hydroxide, NH<sub>3</sub>(ax) = axial NH<sub>3</sub>, NH<sub>3</sub>(eq) = equatorial NH<sub>3</sub>.

where the *x*-axis points from the iron to the pyrimidine, the *y*-axis points from the iron to the deprotonated amide, and the *z*-axis is oriented toward the axial hydroxide ligand (Scheme 6). From the surface plot in Figure 7 it is seen that this orbital is  $\pi$ -antibonding between the iron and the nitrogen of the deprotonated amide. This is an important result and shows that the deprotonated amide is the strongest  $\pi$ -base in the BLM ligand framework. This is also supported by the fact that the iron–amide covalency is the largest within the *t*<sub>2g</sub> set (Table 7). Next in energy is the iron d<sub>xz</sub>-based MO that is oriented toward the imidazole and pyrimidine ligands, but the  $\pi$ -covalency is not particularly large for either ligand (Table 7). Finally, the iron d<sub>xy</sub> orbital is lowest within the *t*<sub>2g</sub> set and has no significant  $\pi$ -interaction with any of the ligands. After a significant energy gap the doubly occupied ligand orbitals follow. As expected from the results of section 3.2 the highest-energy ligand-based orbitals are localized on the deprotonated amide and pyrimidine moieties. The amide orbitals are the most stabilized by bonding to the iron, such that the highest ligand-based orbital is a delocalized  $\sigma$ -orbital that is shared by the amide and pyrimidine ligands, and the next highest is the amide- $\pi$  orbital that was found highest in energy in the free ligand (vide supra, Figure 6).

The Wiberg bond orders are also collected in Table 7 and are sensitive indicators of the metal–ligand bond strength. The strongest bonds are formed between the iron and the two anionic ligands; this mainly reflects the  $\pi$ -bonding contributions from these ligands. The pyrimidine and imidazole ligand–Fe(III) bonds are somewhat less strong, reflecting lower  $\pi$ -donor bonding capabilities, while the amines are the weakest ligands and do not show any significant  $\pi$ -bonding.

In summary the main result of this section is that the nature of the SOMO for Fe(III)BLM in Figure 7 is determined by the  $\pi$ -donor properties of the deprotonated amide that dominates the interaction with the iron-based *t*<sub>2g</sub> orbitals.

**ABLM.** The equivalent scheme for ABLM (8) is shown on the right in Figure 7 and is fairly similar to that obtained for 7. Also, the orbital compositions and Wiberg bond orders collected in Table 8 are similar to the corresponding ones for Fe(III)-BLM (7) in Table 7. As seen from the surface plot (Figure 7, lower right), the SOMO is still  $\pi$ -antibonding between the iron and the deprotonated amide. This is a key result that suggests that the deprotonated amide is a stronger  $\pi$ -donor than the hydroperoxide and therefore dominates over it in determining the nature of the electronic ground state as is also reflected in the Wiberg bond orders in Table 8. It will be shown below that this result is also consistent with all of the observed spectroscopic properties of ABLM. It is this feature, therefore, that distinguishes ABLM from other non-heme iron hydroperoxide complexes<sup>91</sup> that do not have other strong  $\pi$ -donors in their

**Table 8.** Composition of the Iron 3d-based MOs in ABLM (8) and Wiberg Bond Orders for Iron–Ligand Bonding<sup>a</sup>

MO-label	% Fe	% pm	% ad <sup>−</sup>	% iz	% OOH <sup>−</sup>	% NH <sub>3</sub> (ax)	% NH <sub>3</sub> (eq)
d <sub>x<sup>2</sup>−y<sup>2</sup></sub>	64.2	6.3	0.3	4.0	1.5	0.8	6.6
d <sub>z</sub> <sup>2</sup>	68.6	6.6	0.3	0.3	11.4	6.8	5.4
d <sub>yz</sub> SOMO	95.3	0.2	2.1	1.2	0.6	0.4	0.1
d <sub>xz</sub>	97.6	0.6	0.3	0.4	0.1	0.2	0.8
d <sub>xy</sub>	97.2	0.8	0.3	0.3	0.7	0.2	0.5
W <sub>Fe–pm</sub>	W <sub>Fe–ad</sub>	W <sub>Fe–iz</sub>	W <sub>Fe–OOH</sub>	W <sub>Fe–NH3ax</sub>	W <sub>Fe–NH3eq</sub>		
0.636	0.770	0.622	0.654	0.607	0.547		

<sup>a</sup> pm = pyrimidine, ad<sup>−</sup> = deprotonated amide, iz = imidazole, OOH<sup>−</sup> = hydroperoxide, NH<sub>3</sub>(ax) = axial NH<sub>3</sub>, NH<sub>3</sub>(eq) = equatorial NH<sub>3</sub>.

ligand field. Consequently, the ground states of other non-heme iron complexes are dominated by the  $\pi$ -bonding between the iron and the hydroperoxide, whereas in BLM the deprotonated amide dominates in bonding for both Fe(III)BLM and ABLM.

**The *g* Matrix in Fe(III)BLM and ABLM.** The orientation of the SOMO and the ordering of d-orbitals also gives insight into the nature and orientation of the *g* matrix. The largest elements of the *g*-matrix are caused by the most efficient orbital rotations, which are a measure of the efficiency of spin–orbit coupling. The most efficient orbital rotation in Fe(III)BLM occurs between the d<sub>yz</sub> SOMO and d<sub>xz</sub> orbital that is next in energy. This rotation is allowed in the *z*-direction, and therefore the largest element of the *g*-matrix must be oriented approximately toward the hydroxide ligand. The second largest orbital rotation occurs between the d<sub>yz</sub> SOMO and the d<sub>xy</sub> orbital and is allowed in the *y*-direction. The *g*<sub>mid</sub> element of the *g*-matrix must therefore be oriented approximately toward the deprotonated amide ligand. This leaves the pyrimidine–imidazole axis as the *g*<sub>min</sub> direction.

This analysis is supported by numerical calculations based on the INDO/S-CI wave functions and a recently described formalism.<sup>60</sup> Since the excitation energies within the low symmetry-split <sup>2</sup>T<sub>2g</sub> state are so small (below 4000 cm<sup>−1</sup>), they cannot be calculated to high accuracy by electronic structure methods. They were therefore fixed to the energies determined from the ligand field analysis in section 3.2 (the calculated values are within ~1000 cm<sup>−1</sup> of these estimates). The in-state <sup>2</sup>T<sub>2g</sub> contributions are necessarily overestimated since the treatment of ref 60 is based on the validity of second-order perturbation theory; however, the model will give a fairly realistic estimate of the higher energy *t*<sub>2g</sub>→*e*<sub>g</sub> and CT contributions to the *g*-shifts that are neglected in almost all other treatments. The results of the calculations indicate that these contributions are, as expected, fairly small for the *g*<sub>mid</sub> and the *g*<sub>max</sub> shifts. They are 1.7 and 6.6%, respectively, of the total experimentally observed *g*-shifts of Fe(III)BLM (+0.183 and +0.409). For the *g*<sub>min</sub> value, however, a much more important contribution is found that amounts to 72% of the experimentally observed *g*-shift (−0.110). This is likely to be a fairly general result and demonstrates that in many low-spin ferric complexes various multiplets that arise from *t*<sub>2g</sub>→*e*<sub>g</sub> excitations should be included in the interpretation of the *g*<sub>min</sub> shift. Nevertheless, the ligand field parameters *V* and  $\Delta$  can in most cases be estimated from the *g*<sub>mid</sub> and *g*<sub>max</sub> shifts alone.

Since the orbital structure of ABLM is similar to that of Fe(III)BLM, except for small shifts in the <sup>2</sup>T<sub>2g</sub> energies, the same analysis applies, and a similar orientation of the *g* matrix is anticipated and found in the calculations (see Scheme 6).

**Comparison to Mössbauer Results for Fe(III)BLM and ABLM.** The above analysis is substantiated by comparison to



the calculated and measured quadrupole splittings. The measured  $\Delta E_Q$  for Fe(III)BLM is  $-3.0 \pm 0.2$  mm/s.<sup>19</sup> The calculated value for  $\Delta E_Q$  for Fe(III)BLM from the CI wave function is  $-3.07$  mm/s with the largest component of the field gradient along the  $x$ -direction (i.e., along the imidazole–iron–pyrimidine axis), which is also the  $g_{\min}$  direction in our interpretation. The calculated value for ABLM is  $-2.49$  mm/s compared to  $-3.0 \pm 0.2$  mm/s determined experimentally. The same direction of the field gradient tensor for Fe(III)BLM is obtained for ABLM. Importantly, this is in agreement with the experimentally deduced orientation of the field gradient relative to the  $g$  matrix.<sup>19</sup>

**Comparison to  $^{17}\text{O}$  ENDOR Results for ABLM.** Veselov et al. have reported  $^{17}\text{O}$  ENDOR data for ABLM.<sup>22</sup> The largest hyperfine coupling ( $A_{\parallel}(^{17}\text{O}) \approx 27$  MHz) was determined to occur along the  $g_{\text{mid}}$  direction, and smaller couplings ( $A_{\perp}(^{17}\text{O}) \approx 10$  MHz) were observed in the  $g_{\min}$  and  $g_{\max}$  directions. This is consistent with earlier  $^{17}\text{O}$  EPR data that mainly showed broadening of the  $g_{\text{mid}}$  and  $g_{\min}$  features following  $^{17}\text{O}$  substitution.<sup>21</sup> According to our interpretation of the electronic structure of ABLM, the main spin-carrying orbital on the hydroperoxide is the  $\pi^*_{\text{v}}$  orbital which has its lobes oriented parallel to the complex plane. The direction of the two lobes also determines the direction of the spin density field gradient at the coordinating oxygen atom. Therefore, the spin density field gradient has its largest projection in the complex plane and a small projection perpendicular to the plane, that is, along the Fe–O bond direction. This means that, according to the  $g$  matrix orientation proposed above, the largest hyperfine coupling is expected in the  $g_{\text{mid}}/g_{\min}$  plane. The fact that the largest  $^{17}\text{O}$  hyperfine component is experimentally observed along  $g_{\text{mid}}$  would mean that the distal hydroperoxide oxygen should be significantly rotated toward the  $x$ -direction (i.e., along the pyrimidine or imidazole ligands). This is consistent with the computed structure shown in Scheme 6.

In summary, the good agreement between computed and experimentally determined magnetic parameters provides support for the wave functions computed for Fe(III)BLM and ABLM. The  $g_{\max}$  component for both complexes is approximately oriented toward the axial  $\text{OH}^-$  and  $\text{HOO}^-$  ligands, the  $g_{\text{mid}}$  component, approximately toward the deprotonated amide and the  $g_{\min}$  component, approximately toward the pyrimidine ligand.

**3.3.4. Excited Electronic States.** In addition to the ground-state properties, further insight into the excited states of Fe(III)-BLM and ABLM has also been obtained from these calculations. The electronically excited states of doublet multiplicity divide into three categories: (a) the two excited components of the low symmetry-split  $^2\text{T}_{2g}$  ground state where electrons are redistributed within the  $(t_{2g})^5$  configuration; (b) the  $t_{2g} \rightarrow e_g$  excited states in which an electron is promoted from a  $t_{2g}$ -based orbital into an  $e_g$  orbital; and (c) the LMCT excited states in which an electron is promoted from a ligand-based orbital into a metal-based orbital. The states of categories (a) and (b) have been dealt with at length in sections 3.2 and require little further analysis.

**Fe(III)BLM.** The computed spectrum of Fe(III)BLM (7) is documented in Table 9. In agreement with the interpretation of the experimental spectrum the calculations predict the three components of the low symmetry-split  $^2\text{T}_{2g}$  ground state to be below  $5000\text{ cm}^{-1}$ . The exact positions of these states are difficult to calculate with high accuracy, and therefore they have been fixed to the estimates from the ligand field analysis. Next in energy the calculations predict a series of  $t_{2g} \rightarrow e_g$  d–d excited

**Table 9.** Calculated ABS Spectrum for Fe(III)BLM (7) up to  $30\,000\text{ cm}^{-1}$  and Assignments

energy ( $\text{cm}^{-1}$ )	$f_{\text{osc}} \times 10^4$	assignment
1850 <sup>a</sup>	0.08	$d_{xz} \rightarrow d_{yz}$
3900 <sup>a</sup>	0.05	$d_{xy} \rightarrow d_{yz}$
18 010	1.8	$t_{2g} \rightarrow e_g$
18 800	3.0	$t_{2g} \rightarrow e_g$
19 400	12.0	$t_{2g} \rightarrow e_g$
21 940	0.3	$t_{2g} \rightarrow e_g$
22 620	3.2	$t_{2g} \rightarrow e_g$
23 300	2.4	$t_{2g} \rightarrow e_g$
24 510	33.3	pyrimidine/amide $\rightarrow d_{yz}$ $\sigma$ -LMCT
25 510	38.9	$t_{2g} \rightarrow e_g$
26 060	59.5	$t_{2g} \rightarrow e_g$
26 380	268	amide $\rightarrow d_{yz}$ $\pi$ -LMCT
26 490	4.5	$t_{2g} \rightarrow e_g$
26 640	2.0	$t_{2g} \rightarrow e_g$
27 490	7.7	$t_{2g} \rightarrow e_g$
27 560	0.7	$t_{2g} \rightarrow e_g$
28 070	1.2	$t_{2g} \rightarrow e_g$
31 470	0.4	$t_{2g} \rightarrow e_g$

<sup>a</sup> Adjusted to values determined by the ligand field analysis.

states with fairly low absorption intensities, again in agreement with experiment. The first  $t_{2g} \rightarrow e_g$  excited state is computed at  $18\,010\text{ cm}^{-1}$  and experimentally found at  $16\,640\text{ cm}^{-1}$ . Thus, the calculations are only in error by  $\sim 1500\text{ cm}^{-1}$ , and this error should be relatively uniform for the remaining  $t_{2g} \rightarrow e_g$  excited states. The ligand field analysis presented in section 3.2 gives the most insight into the ligand field excited states, and therefore further comparisons for individual  $t_{2g} \rightarrow e_g$  excited states are not necessary here.

The most interesting question for the MO calculations is the nature of the orbitals that give rise to the LMCT excitations. The key to the interpretation of the experimental LMCT data is provided by the first two LMCT transitions. These two states are predicted at  $24\,510$  and  $26\,380\text{ cm}^{-1}$ . The second LMCT state is by far the strongest transition with a predicted oscillator strength,  $f_{\text{osc}}$ , of 0.027, whereas the first is predicted to be almost an order of magnitude weaker with an  $f_{\text{osc}}$  of 0.003. The second LMCT state is assigned to band 11 that corresponds to the absorption maximum of Fe(III)BLM in Figure 1 and was experimentally found at  $26\,270\text{ cm}^{-1}$  (Table 1). The first LMCT state most likely belongs to band 9 or 10 in the experimental spectrum that were experimentally found at  $24\,470$  and  $25\,330\text{ cm}^{-1}$  (Table 1).

The nature of the excitations is most conveniently analyzed through the NOs of the individual states. For the ground state and the two LMCT states under investigation there is a single NO with an occupation number close to 1.0. The ground-state SOMO corresponds to the acceptor MO, and the excited-state SOMO corresponds to the donor MO in the LMCT transition. Surface plots of the NOs are shown in Figure 8. It is seen from the figure that the first LMCT transition originates from a  $\sigma$ -orbital that is delocalized over the pyrimidine and the deprotonated amide moieties. This transition is relatively weak because it has a poor transition dipole moment with the acceptor MO (Table 9). The delocalized nature of the donor MO accounts for the observation in the rR spectrum (section 3.1.1) that the vibrational modes of both the pyrimidine and the deprotonated amide are enhanced with excitation energies in the  $25\,000\text{ cm}^{-1}$  region. It cannot be concluded, however, that the delocalized nature of this NO reflects a strong conjugation between the pyrimidine and the deprotonated amide in the ground state of Fe(III)BLM because this would involve the  $\pi$ -system and not the  $\sigma$ -system that is the case here.

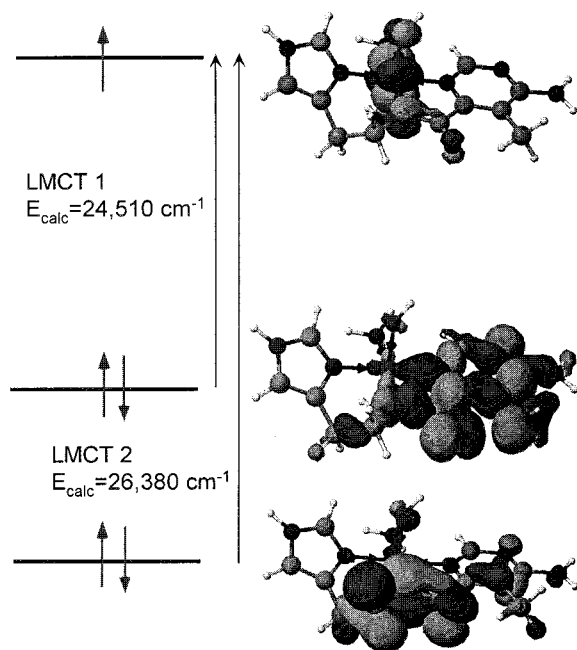


**Figure 8.** Approximate NOs of the ground state of Fe(III)BLM (7) and the first two LMCT excited states.

The much more intense LMCT transition that is assigned to band 11 in the experimental spectrum and that dominates the resonance enhancement of the Raman spectrum originates from a  $\pi$ -MO that is almost exclusively localized on the deprotonated amide (LMCT 2 in Figure 8). This donor MO has a large transition dipole moment with the ground state SOMO because they form a bonding/antibonding pair (Table 9). The intensity of this transition in the experimental spectrum is further evidence for the orientation of the ground state SOMO deduced in the previous section. This excited state should primarily give rise to rR enhancement of the deprotonated amide vibrational modes. Unfortunately, the rR data could not be extended beyond 26 380  $\text{cm}^{-1}$  due to decomposition and fluorescence problems, and therefore it is possible that the two LMCT transitions described above both contribute to the observed rR enhancements.<sup>95</sup> Beyond the first two LMCT states the density of states rapidly increases; additionally, the very intense intraligand  $\pi \rightarrow \pi^*$  transitions mask further LMCT transitions.

**ABLM.** The most obvious change in the optical properties of ABLM relative to Fe(III)BLM is the prominent MCD band 2 in the region around 16 500  $\text{cm}^{-1}$  that was studied in some detail in section 3.1.2. The calculations give insight into the nature of this band. The calculated spectrum summarized in Table 10 shows the onset of  $t_{2g} \rightarrow e_g$  excitations with very low intensity at 16 320  $\text{cm}^{-1}$  compared to 16 940  $\text{cm}^{-1}$  deduced experimentally (Table 2). The next three excited states are all computed in the range 19 100–19 500  $\text{cm}^{-1}$ . Two of them are also  $t_{2g} \rightarrow e_g$  excitations and are calculated with low intensity, while the third transition in this region is the first LMCT state. The natural orbital analysis in Figure 9 shows that this is a LMCT transition from the peroxide  $\pi^*_v$  orbital into the iron  $d_{yz}$ -based SOMO. Since this transition results from the axial hydroperoxide ligand it is calculated to be  $z$ -polarized. The transition, however, has very low intensity due to the poor relative orientation of the hydroperoxide  $\pi$ -donor and the

**Table 10.** Calculated ABS Spectrum for ABLM (8) up to 30 000  $\text{cm}^{-1}$  and Assignments

energy ( $\text{cm}^{-1}$ )	$f_{\text{osc}} \times 10^4$	assignment
2800 <sup>a</sup>	0.3	$d_{xz} \rightarrow d_{yz}$
4200 <sup>a</sup>	0.6	$d_{xy} \rightarrow d_{yz}$
16 320	0.2	$t_{2g} \rightarrow e_g$
19 120	15.2	$t_{2g} \rightarrow e_g$
19 350	25.3	$t_{2g} \rightarrow e_g$
19 510	13.0	peroxide $\pi^*_v \rightarrow d_{yz}$ $\pi$ -LMCT
20 800	2.1	$t_{2g} \rightarrow e_g$
21 880	4.5	$t_{2g} \rightarrow e_g$
23 460	13.6	$t_{2g} \rightarrow e_g$
23 830	23.7	pyrimidine/amide $\rightarrow d_{yz}$ $\sigma$ -LMCT
24 570	132	$t_{2g} \rightarrow e_g$ + LMCT
25 190	17.4	$t_{2g} \rightarrow e_g$
25 470	247	$\pi^*_v \rightarrow d_{yz}$ LMCT
26 020	16.7	$t_{2g} \rightarrow e_g$
26 560	95	$t_{2g} \rightarrow e_g$
27 030	70	$t_{2g} \rightarrow e_g$
27 080	81	$t_{2g} \rightarrow e_g$
27 250	108	amide $\rightarrow d_{yz}$ $\pi$ -LMCT + $\pi^*_s \rightarrow d_{yz}$ LMCT
27 850	48	$t_{2g} \rightarrow e_g$
28 740	3.5	$t_{2g} \rightarrow e_g$
29 220	169	$t_{2g} \rightarrow e_g$ + LMCT
29 980	38	$t_{2g} \rightarrow e_g$
30 530	124	pyrimidine/amide $\rightarrow d_{x^2-y^2}$ $\sigma$ -LMCT

<sup>a</sup> Adjusted to values determined by the ligand field analysis.

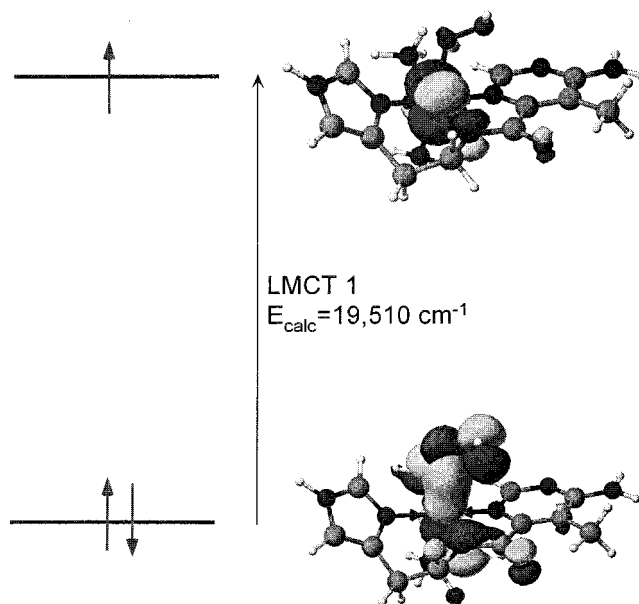


**Figure 9.** Approximate NOs of the ground state of ABLM (8) and the first LMCT excited state.

Fe- $d_{yz}$  acceptor MOs. We assign the band experimentally characterized around 16 940  $\text{cm}^{-1}$  (band 2 in Figures 3 and 4) to this cluster of three transitions. The MCD data show that there is strong polarization in the  $g_{\text{max}}$  direction in this region that varies over the envelope of the band. Consequently, there must be more than one electronic transition associated with band 2 in the experimental spectrum. According to our interpretation of the  $g$  matrix in section 3.3.3 and Scheme 6, the  $g_{\text{max}}$  direction coincides with the iron–hydroperoxide direction, and therefore the  $z$ -polarized intensity can be assigned to the LMCT transition in this region. The remaining intensity was experimentally found to be polarized mainly along the  $g_{\text{mid}}$  direction that coincides with the iron–amide direction, and this also agrees with the calculated polarizations for the two  $t_{2g} \rightarrow e_g$  excitations in this region. The striking feature of this assignment is the very low ABS intensity associated with the peroxide-to-iron  $\pi$ -LMCT.

(95) It is also possible that other d–d excited states and the first LMCT transition borrow intensity from this transition to a greater extent than present in the calculations through vibronic coupling mechanisms that have not been included in the theoretical model.

In other low-spin hydroperoxide–Fe(III) complexes this transition is also found in this energy region but is much more intense.<sup>91</sup> In these complexes the donor and acceptor MOs are suitably oriented to give a large transition dipole moment.<sup>85</sup> This again emphasizes the crucial role of the deprotonated amide in the BLM ligand framework. This dominates over the  $\pi$ -bonding capabilities of the hydroperoxide and therefore orients the SOMO so as to reduce the overlap of the hydroperoxide  $\pi^*_v$  orbital with the  $t_{2g}$  hole that quenches the hydroperoxide-to-iron  $\pi$ -LMCT intensity. The low CT intensity implies reduced  $\pi$ -donor interactions of the hydroperoxide in ABLM consistent with the ligand field analysis presented in section 3.2. The ABS spectrum of ABLM in the region 20 000–30 000  $\text{cm}^{-1}$  largely parallels that of Fe(III)BLM but probably contains some additional peroxide-to-iron LMCT character (Table 10).

**Summary.** The calculations have generated an electronic structure description that is consistent with all spectroscopic data for Fe(III)BLM and ABLM. According to this description the iron–ligand bonding in both complexes is dominated by the strong bond between the iron and the amide, which becomes a strong  $\pi$ -donor upon deprotonation. Therefore, the deprotonated amide determines the orientation of the redox-active orbital in these low-spin ferric complexes and also the magnetic axes (Scheme 6). The optical spectra mainly reflect a strongly allowed deprotonated amide-to-iron LMCT transition with some contribution from a weakly allowed transition originating from a delocalized pyrimidine/amide  $\sigma$ -orbital that occurs at somewhat lower energy. The delocalization of this orbital is consistent with the rR results. It does *not*, however, reflect strong conjugation of the deprotonated amide and pyrimidine moieties because this would require electron delocalization over the  $\pi$ -system. Such  $\pi$ -delocalization appears to be a minor factor in Fe(III)BLM and ABLM. In ABLM the hydroperoxide ligand gives rise to a very weak, low-energy LMCT transition that is experimentally defined by the VTVH MCD polarization study (section 3.1.2, Figure 4). This transition is very weak in absorption because the hydroperoxide  $\pi^*_v$  donor orbital has poor overlap with the hole in the iron  $t_{2g}$ -based orbital set since the hole orientation is determined by the  $\pi$ -antibonding interaction with the deprotonated amide. The hydroperoxide is therefore a relatively poor  $\pi$ -donor ligand in ABLM.

**3.4. Electronic Structure Calculations: Reactivity. Possible Pathways.** Given reasonable and experimentally substantiated electronic structure descriptions of Fe(III)BLM and ABLM, further calculations were carried out to gain insight into the question of the reactive species in BLM chemistry that attacks DNA. The accepted mode of reactivity is a hydrogen-atom abstraction from the C4' position of the DNA ribose sugar. Three possible scenarios were considered: (a) heterolytic cleavage of the O–O bond that would lead to a high-valent, formally Fe(V)=O, intermediate that attacks DNA; (b) homolytic cleavage of the O–O bond that would lead to an OH radical and a high-valent, formally Fe(IV)=O, intermediate both of which could attack DNA; and (c) direct reaction of the low-spin Fe(III)–OOH species with DNA to give a DNA radical,  $\text{H}_2\text{O}$  and an Fe(IV)=O species. To date no unambiguous data have been reported that would allow one to distinguish the actual mechanism of DNA cleavage. As is the case in cytochrome P450 chemistry, the reactive species may be very short-lived and may not build up to sufficient levels for direct detection.<sup>96</sup>

**3.4.1. Heterolytic Cleavage.** The hypothetical heterolysis of the O–O bond in ABLM can be written as:

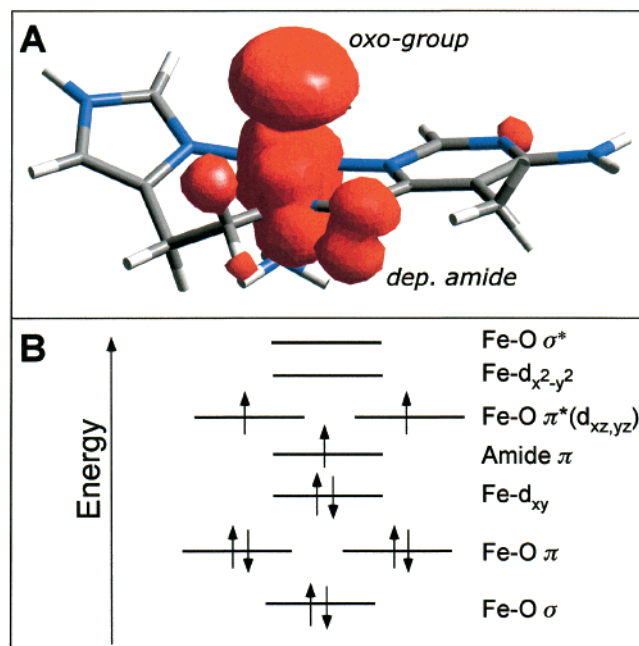
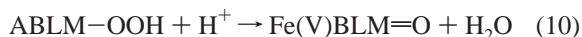


**Figure 10.** Electronic structure of the hypothetical Fe(V)BLM=O. (A) Total spin density for the  $M_S = 3/2$  state from an unrestricted BPW91 DFT calculation. (B) Qualitative MO diagram derived from the calculations.

Thus, on the reactant side ABLM and a proton are required, and the cleavage products are a formally Fe(V)–oxo species of BLM and a water molecule. The analysis of this hypothetical reaction proceeds by comparing the electronic and geometric structures of ABLM and the hypothetical Fe(V)BLM systems and then estimating the reaction energy from DFT calculations. Finally the differences between cytochrome P450 and BLM will be considered.

**Electronic Structure of Fe(V)BLM=O.** A number of resonance structures can be formulated for complexes with the formal description Fe(V)=O:  $\text{Fe(V)O}(-\text{II})\text{L} \leftrightarrow \text{Fe(IV)O}(-\text{I})\text{L} \leftrightarrow \text{Fe(III)O}(0)\text{L} \leftrightarrow \text{Fe(IV)O}(-\text{II})\text{L}^+ \cdot$  etc., where L denotes the ligand framework. Thus, apart from the electron distribution over the iron and oxygen atoms, an electron may also be ionized from a ligand orbital such that a radical species is obtained. The latter situation is found in compound I analogues of high-valent iron–oxo porphyrins that on the basis of Mössbauer experiments are best described as  $(\text{FeO})^{2+}\text{P}^-\cdot$ .<sup>97</sup> Thus, one of the two electrons that are involved in the redox process is taken from the iron and one from the porphyrin ring in the creation of compound I.

Figure 10A shows the total spin density computed from BPW91 DFT calculations for the  $M_S = 3/2$  state of the hypothetical Fe(V)BLM=O species. It is seen that the spin is not only localized on the iron and oxygen atoms but that there is also a large spin density on the deprotonated amide. This shows that in Fe(V)BLM=O the situation is similar to that found in compound I, namely that the removal of the second electron occurs from a ligand and not from a metal orbital. This result also reinforces the conclusion in section 3.3.1 that electron

(96) However, most recently direct experimental evidence for the postulated intermediates of the reaction in cytochrome P450cam has been obtained. Schlichting, I.; Berendzen, J.; Chu, K.; Stock, A. M.; Maves, S. A.; Benson, D. E.; Sweet, R. M.; Ringe, D.; Petsko, G. A.; Sligar, S. G. *Science* **2000**, *287*, 1615.

(97) (a) Ruttger, R.; Hager, L. P.; Dhonau, H.; Hendrich, M.; Valentine, M.; Debrunner, P. *Biochemistry* **1984**, *23*, 6809. (b) Ruttger, R.; Hager, L. P. *J. Biol. Chem.* **1982**, *257*, 7958. (c) Antony, J.; Grodzicki, M.; Trautwein, A. X. *J. Phys. Chem.* **1997**, *101*, 2692.



delocalization over the pyrimidine and deprotonated amide  $\pi$  systems is not a major factor in the electronic structure of BLM.

The result can be understood from the qualitative MO diagram in Figure 10B. Starting from the low-spin Fe(III) electronic structure description of ABLM in Figure 7, the conversion to Fe(V)BLM=O proceeds by removal of one electron from the iron- $d_{xz}$  orbital and one electron from the amide- $\pi$  orbital that becomes the highest ligand-based MO in the oxo species. There is a strong  $\pi$ -interaction between the iron- $d_{xz,yz}$  and the oxo- $p_{x,y}$  orbitals that leads to a large splitting of the  $d_{xy}$  and  $d_{xz,yz}$  orbitals on the iron. Two very covalent sets of orbitals are therefore formed that are designated Fe–O  $\pi$ , which are doubly occupied and bonding, and Fe–O  $\pi^*$ , which are both singly occupied and antibonding. From the electron count this leaves one net  $\pi$ -bond between the iron and the oxo group. Lower in energy is the doubly occupied Fe–O  $\sigma$ -bonding MO that is formed from the iron- $d_{z^2}$  and oxo- $p_z$  orbitals. The antibonding Fe–O  $\sigma^*$  counterpart is higher in energy and unoccupied which leaves one net  $\sigma$ -bond between the iron and oxo groups. The increased effective nuclear charge on the iron due to removal of another electron from the low-spin  $d^5$  configuration leads to further stabilization of the iron d-manifold relative to the ligand orbitals. As a consequence the iron- $d_{xy}$  orbital becomes lower in energy than the highest ligand-based orbital. Therefore, the iron- $d_{xy}$  orbital, which has no strong bonding or antibonding interaction with any ligand orbital, stays doubly occupied, and the additional hole is created on the deprotonated amide. This ordering requires that the amide- $\pi$  and delocalized pyrimidine- $\sigma$  orbitals characterized in section 3.3.3 and Figure 7 exchange their energetic position in the ligand manifold. This is consistent with a decreased  $\pi$ -bonding interaction between the oxidized deprotonated amide and the iron and leads to less stabilization of the deprotonated amide  $\pi$  orbital.

Various multiconfigurational calculations were also carried out at the INDO/S level for the equilibrium geometry. An active space full CI calculation based on a configuration averaged Hartree–Fock (CAHF(9,6)) SCF reference was used to estimate the energies of different spin states. The calculations predict an  $S = 1/2$  ground state very close in energy (within  $200\text{ cm}^{-1}$ ) to the  $S = 3/2$  state described above. The lowest  $S = 1/2$  state is mainly characterized by an antiferromagnetic coupling between the  $\{\text{FeO}\}^{2+}$  core with  $S = 1$  and the hole on the deprotonated amide with  $S = 1/2$ . Since there is no experimental number for this quantity and the computed values are also subject to some change upon enlarging the CI space, no further attempt was made to compute a more accurate number for the doublet–quartet splitting. The prediction of antiferromagnetic coupling leading to a  $S = 1/2$  ground state is consistent with the situation found for compound I models in high-valent iron–oxo porphyrin chemistry<sup>97</sup> and does not change the basic description of the bonding developed above.

**Estimate of Reaction Energetics.** To estimate the energetics of the heterolytic cleavage reaction B3LYP calculations were performed. One crucial point of these calculations concerns the source of the proton required for the cleavage product  $\text{H}_2\text{O}$ . It is clearly not appropriate to take a naked proton with electronic energy zero as the reference because the proton has a very large solvation energy. A recent high-quality theoretical study<sup>98</sup> gives a value of  $-262.23\text{ kcal/mol}$  for this number, which is in excellent agreement with the upper bound of the experimental estimate of  $-257 \pm 5\text{ kcal/mol}$ .<sup>99</sup> Using this theoretical value for the proton hydration energy, a reaction energy of  $+78.5$

kcal/mol results at the B3LYP level for the heterolytic O–O bond cleavage in ABLM.<sup>100</sup> The difference in solvation energy of the oxo and hydroperoxo species was estimated to be  $\sim 12.5\text{ kcal/mol}$  in favor of the oxo species by a simple Born model and therefore does not change the basic picture. Thus, the reaction is predicted to be considerably uphill and therefore is unlikely to play a major role in BLM chemistry.

**Comparison to Cytochrome P450.** Using the same methodology and basis sets, the analogous reaction of peroxy-P450 to compound I was evaluated. A reaction energy of  $-78.3\text{ kcal/mol}$  was obtained. Thus, the reaction is predicted to be highly favorable, which is consistent with the generally accepted idea that heterolytic O–O bond cleavage plays a major role in cytochrome P450 chemistry. This is in agreement with, but quantitatively different from, the number obtained in a recent DFT study of the same reaction.<sup>101</sup> The majority of the energy difference is that the naked proton was taken as the proton source in ref 100, whereas in this study the hydration energy of the proton was taken into account.

The main result of these computations is that, unlike the situation found in cytochrome P450, the heterolytic bond cleavage in ABLM is predicted to be very unfavorable and, in fact, is unlikely to be significant for the DNA cleavage mechanism of BLM. This result is at variance with much of the speculations in the literature that postulate analogous mechanisms for cytochrome P450 and BLM. Further insight into the differences between these systems comes from comparison of the electronic structures of cytochrome P450 and BLM and their CT spectra to be presented in the discussion.

**Summary.** The main finding of this section is that the heterolytic O–O bond cleavage in ABLM breakdown that would produce a high-valent, formally Fe(V)–oxo species is predicted to be energetically too unfavorable to contribute to ABLM chemistry. Importantly, this high-valent species, like cytochrome P450 compound I, is best described as an Fe(IV)=O unit magnetically coupled to a ligand radical with the ligand hole essentially localized on the deprotonated amide.

**3.4.2. Homolytic Cleavage.** The alternative homolytic cleavage of the O–O bond in ABLM can be written:



This reaction directly yields the compound II analogue of BLM and an OH radical. The same electronic structure study was carried out on the hypothetical Fe(IV)BLM=O as described above for Fe(V)BLM=O. The electronic structure of Fe(IV)BLM=O can be easily understood from the results for Fe(V)BLM=O shown in Figure 10. The extra electron present in Fe(IV)BLM=O enters the lowest-energy available orbital, the deprotonated amide  $\pi$  orbital. This leaves a highly covalent  $\{\text{FeO}\}^{2+}$  core with a very similar orbital structure as described for Fe(V)BLM=O above and a total spin of  $S = 1$  that arises from having the two Fe=O  $\pi^*$ -orbitals singly occupied with parallel spins.

The reaction energetics were again estimated from B3LYP calculations to be  $+24\text{ kcal/mol}$ . At the present level of modeling this number is not considered to be a strong argument against the thermodynamic feasibility of the reaction.

Nevertheless, there are at least two arguments against this formulation of ABLM chemistry. First, it is frequently argued

(100) The B3LYP calculations on the oxo species were carried out for the  $M_S = 3/2$  state, which is computationally more convenient and introduces a negligible error relative to a calculation of the antiferromagnetically coupled  $M_S = 1/2$  state.

(101) Harris, D. L.; Loew, G. H. *J. Am. Chem. Soc.* **1998**, *120*, 8941.

(98) Tawa, G. J.; Topol, I. A.; Burt, S. K. *J. Chem. Phys.* **1998**, *109*, 4852.

(99) Marcus, R. A. *Ion Solvation*; Wiley-Interscience: New York, 1985.

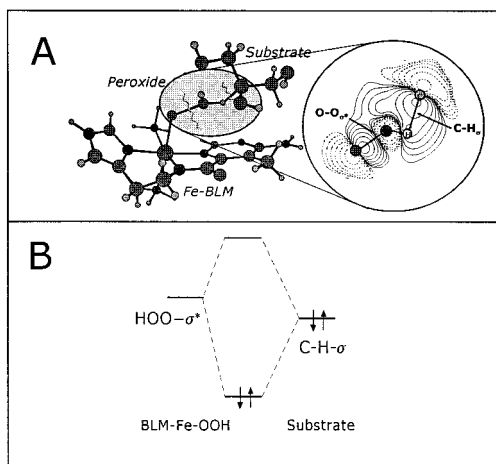
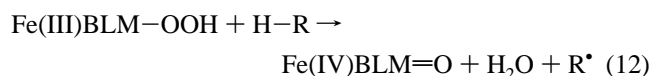


**Figure 11.** Theoretical model for the direct attack of the peroxide in ABLM on the C-H bond of the DNA substrate. (A) The geometric model used with both the peroxide O-O bond and the substrate C-H bond stretched to 1.75 Å. The contour shown is the “active” UHF-NO. (B) Qualitative MO diagram illustrating the interaction between the peroxide  $\sigma^*$  and the C-H- $\sigma$  bond orbital.

that free hydroxide radicals are unlikely to be involved in the reaction because they would show indiscriminate reactivity, while that observed for BLM is highly specific.<sup>4,5,6</sup> The second argument concerns the kinetics of the cleavage reaction. It has been speculated that homolytic O-O bond cleavage will have a very high activation barrier.<sup>102</sup> This has also been observed in preliminary DFT calculations where the O-O bond in ABLM has been stretched (results not shown). Additional evidence will be presented in the discussion.

**3.4.3. H-Atom Abstraction by Hydroperoxide-Fe(III)-BLM.** The alternative to the presence of either a high-valent, formally Fe(V)=O species or hydroxyl radicals as the active species in BLM chemistry is the direct reaction of the bound hydroperoxide in ABLM with DNA. This reaction is written:



With glycerol as a model substrate the calculated reaction energy using B3LYP is  $\sim +14$  kcal/mol which is considered close enough to zero for the reaction to be feasible at the present level of modeling.

In such a reaction the transition state would contain contributions from O-O as well as from C-H bond breaking. The theoretical modeling of such a transition state is a very involved task that is outside the scope of this study. However, we have qualitatively investigated a model for this reaction to obtain some idea about the relevant orbital interactions. Glycerol was chosen as a model substrate, and the central C-H bond was oriented to approach the OH group of the bound hydroperoxide at a reasonable angle of 120°. To qualitatively simulate a transition state both the C-H bond and the O-O bond were stretched from their equilibrium distances to 1.75 Å. The UHF-INDO/S model was chosen for a theoretical method, and the NOs of the UHF wave function were analyzed. The NOs with fractional occupation (i.e., not close to 2 or 0) are the orbitals that are “active” in the reaction.<sup>104</sup> Figure 11A shows the geometric model used in the calculations together with the highest-energy active ligand orbital. This orbital has an occupa-

**Table 11.** Equilibrium Distances and Force Constants from Morse Fits to Calculated O-O Potential Energy Surface for Several Peroxide Species<sup>a</sup>

	spin	method	$R_{\text{eq}}$ (Å)	$k$ (mdyn/Å)
ABLM (8)	$1/2$	BPW91	1.610	2.38
[Fe(NH <sub>3</sub> ) <sub>5</sub> (OOH)] <sup>2+</sup>	$1/2$	BPW91	1.545	2.59
		MP2	1.573	3.57
[Fe(NH <sub>3</sub> ) <sub>5</sub> (OOH)] <sup>2+</sup>	$5/2$	BPW91	1.514	3.28
		MP2	1.452	5.09
H <sub>2</sub> O <sub>2</sub>	0	BPW91	1.541	3.57
		MP2	1.445	4.90

<sup>a</sup> The surfaces were calculated under “rigid” conditions, i.e., the O-O bond was elongated without changing any other structural parameter.

tion close to 2.0 and it is  $\sigma$ -antibonding between the two peroxide oxygens and C-H bonding. An interpretation of this result is shown in Figure 11B. The hydroperoxide  $\sigma^*$  orbital is deep in energy in ABLM. Upon elongation of the O-O bond, this empty orbital can interact with the doubly occupied C-H  $\sigma$ -bonding orbital such that electron density is transferred from the C-H  $\sigma$  bond to the hydroperoxide. This weakens both the O-O bond and the C-H bond because electron density is taken from a C-H bonding orbital and placed into a O-O antibonding orbital. Consequently, further elongation of both bonds will be progressively easier up to the point where both bonds are broken and the products are released. In this way one can envision a reaction that cleanly and directly proceeds from ABLM and DNA to the products Fe(IV)BLM=O, H<sub>2</sub>O, and a DNA radical without invoking a high-valent intermediate or free hydroxyl radicals.

A prerequisite for this model is a relatively low-lying peroxide  $\sigma^*$  orbital for the interaction with the C-H- $\sigma$  bond to be feasible. The present and related calculations<sup>103</sup> are consistent with the idea that this is a general feature of protonated peroxides since the effect of protonation is to remove electron density from the peroxide. Consequently, all peroxide orbitals are substantially lowered in energy, and therefore the peroxide becomes much more electrophilic than in the unprotonated state. This is also consistent with the calculations on ABLM described in section 3.3 where the peroxide  $\sigma^*$  orbital was close in energy to the unoccupied iron  $e_g$  orbitals (not shown). This result also sharply contrasts with our previous experimental and theoretical results for the unprotonated peroxide in [Fe(EDTA)(O<sub>2</sub>)]<sup>3-</sup> which concluded that in the side-on ferric peroxide complex the peroxide  $\sigma^*$  orbital is high in energy and not available for back-bonding.<sup>105</sup>

**Nature of the O-O Bond.** The interpretation presented in the preceding sections implies a relatively weak O-O bond in ABLM. To obtain more insight into this result, further calculations were carried out for two [Fe(NH<sub>3</sub>)<sub>5</sub>(OOH)]<sup>2+</sup> model complexes with  $S = 1/2$  and  $S = 5/2$ . The variation of the total energy with the O-O bond length was calculated by BPW91 DFT calculations and the Hartree-Fock-based RMP2 method. In addition the ABLM model described in section 3.3 was investigated with the BPW91 DFT method. The resulting surface was least-squares fit to a Morse potential, and the O-O force constant was extracted from the fit as a measure of bond stiffness.

From the results in Table 11 it is evident that the DFT and MP2 results both show the same trend but differ in the absolute

(102) Solomon, E. I.; Sundaram, U. M.; Machonkin, T. E. *Chem. Rev.* **1996**, *96*, 2563.

(103) Root, D. E.; Mahroof-Tahir, M.; Karlin, K. D.; Solomon, E. I. *Inorg. Chem.* **1998**, *37*, 4838.

(104) In the ab initio context UHF-NOs were used by Pulay and co-workers to define a UNO-CAS method that closely parallels the results of CASSCF calculations but is computationally much less demanding. The UHF-NOs are also a convenient starting point for defining CASSCF active spaces. Pulay, P.; Hamilton, T. P. *J. Chem. Phys.* **1988**, *88*, 4926.

(105) Neese, F.; Solomon, E. I. *J. Am. Chem. Soc.* **1998**, *120*, 12829.

magnitude of the predicted force constants. As expected, the MP2 values are consistently larger than the DFT values. Interestingly, upon going from the high-spin,  $S = 5/2$ , hydroperoxide complex to the low-spin form, the O—O bond gets longer and much less stiff as evidenced by a 20–30% decrease in the force constant of this bond. While the O—O bond in the high-spin complex is comparable to that of hydrogen peroxide calculated at the same level of theory, the O—O bond in the low-spin complex appears to be much weaker, in agreement with a recent experimental study.<sup>91a,85</sup> Importantly, the calculations predict that the O—O bond in ABLM is even weaker and longer than that found in the non-heme iron low-spin hydroperoxide complex. This is consistent with the analysis described above and the fact that the  $\text{HOO}^- \pi^*_{\text{v}}$  orbital is a poor donor in ABLM due to the deprotonated amide orientation of the  $d_{yz}$  acceptor orbital. It also gives further evidence that the mechanism proposed is reasonable. The O—O bond in ABLM is therefore easily elongated from an already very long equilibrium distance, and this will shift the O—O  $\sigma^*$  orbital down in energy such that it can readily interact with the substrate C—H bond which would result in the cleavage of both bonds.

#### 4. Discussion

The present study has focused experimentally and theoretically on the spectroscopic properties and the electronic structure of ABLM and its precursor, the low-spin ferric form of the drug (Fe(III)BLM). In a second step, possible mechanisms for the reaction of ABLM with DNA were theoretically evaluated.

The geometric structures of both Fe(III)BLM and ABLM are closely analogous and consistent with the structure of the Co(III)OOH derivative studied by Stubbe and co-workers<sup>8–10</sup> and others.<sup>106</sup> In this model the pyrimidine, deprotonated amide, imidazole, and primary amine functionalities are ligands to iron, and all approximately reside in a plane. The axial ligands are an amine from the  $\beta$ -aminoalanine group of BLM and an  $\text{OH}^-$  in Fe(III)BLM. An  $\text{OOH}^-$  replaces  $\text{OH}^-$  as a sixth ligand in ABLM.

On the basis of our results, the key feature in the bonding of both Fe(III)BLM and ABLM is the deprotonated amide ligand. After deprotonation the amide functionality becomes very basic and dominates the ligand field of the low-spin ferric site. The deprotonated amide is also the ligand that has the strongest  $\pi$ -interaction with the iron  $t_{2g}$ -based orbitals. Consequently, this ligand determines the orientation of the SOMO in the low-spin  $t_{2g}^5$  configuration and therefore most of the ground-state properties. A perhaps surprising feature is that the deprotonated amide also dominates over the hydroperoxide in ABLM, and therefore ABLM is different from other non-heme low-spin ferric hydroperoxide complexes, where the peroxide dominates the ligand field.<sup>90,93</sup>

**Electronic Structure and Spectroscopy.** On the basis of this description, both the ground- and excited-state spectral features of Fe(III)BLM and ABLM are readily understood. Due to the particular orientation of the hole in the  $t_{2g}$  set, the largest  $g$ -value is oriented toward the axial ligand, the intermediate  $g$ -value, along the iron deprotonated amide bond, and the smallest

$g$ -value, approximately along the iron pyrimidine bond (Scheme 6). The analysis also shows that all three  $g$ -values must be positive. In fact, in this study Griffith's ligand field model<sup>79,80</sup> for the  $g$ -values of low-spin  $d^5$  species was put to an experimental test. Through direct observation of the highest intra- $t_{2g}$  transition it was found that this model gives good agreement between experiment and theory unlike the situation found with Griffith's model for the zero-field splittings of high-spin  $d^5$  species.<sup>60</sup>

The ligand field analysis of Fe(III)BLM and ABLM in section 3.2 shows that both species have a very similar ligand field with only minor shifts in the energy levels due to the replacement of the hydroxide by a hydroperoxide ligand. Both Fe(III)BLM and ABLM are relatively close to the crossover point between high- and low-spin complexes ( $10Dq \approx 20\,000\text{ cm}^{-1}$ ). In fact, high-spin Fe(III)BLM is found at low pH or in phosphate buffer.<sup>107</sup> On the basis of this analysis the complicated low-energy part of the ABS, CD, and MCD spectra is well understood as arising from the various doublets associated with  $t_{2g} \rightarrow e_g$  excitations within the iron 3d shell.

The ABS spectrum with a peak around 386 nm has been shown in this study to consist of a complex series of electronic transitions. On the basis of rR spectroscopy and electronic structure calculations, the main sources of intensity in this region are LMCT transitions from the deprotonated amide to the  $t_{2g}$  hole of the ferric iron. Consequently, intra-amide vibrations are strongly resonance-enhanced, and the transitions are reasonably intense due to favorable orbital orientation. These observations therefore provide experimental insight into the bonding picture derived from electronic structure calculations. The complex vibrational patterns observed in the rR spectra of Fe(III)BLM can be concisely interpreted as arising from vibrations localized on the deprotonated amide and pyrimidine functionalities, and some reassignments have been suggested.

The combined experimental and theoretical analysis obtained from these studies has generated an electronic structure description that distinguishes BLM from other biological non-heme iron centers. The key difference relative to other non-heme iron sites is the presence of a highly basic  $\pi$ -donor ligand, the deprotonated amide that is lacking in more conventional biological ligand fields, which are dominated by histidine and carboxylate side chains. Thus, BLM occupies a position intermediate between the very electron-rich heme centers and non-heme iron sites with much poorer donor ligands. This study, however, shows that there is little, if any, of the conjugation between the deprotonated amide and pyrimidine functionalities that was previously postulated to lead to efficient electron delocalization over these two moieties. In particular, an important result of this study is that such delocalization does *not* occur.

Given this experimentally substantiated electronic structure description of Fe(III)BLM and ABLM, the reactivity of FeBLM toward DNA was approached theoretically. Three possibilities were considered: (a) the O—O bond is cleaved heterolytically to give the compound I analogue  $\text{Fe(V)BLM}=\text{O}$ ; (b) the O—O bond in ABLM breaks homolytically to give  $\text{Fe(IV)BLM}=\text{O}$  and a hydroxyl radical; and (c) ABLM directly reacts with DNA to give  $\text{Fe(IV)BLM}=\text{O}$ , a DNA radical and water. The study of the three possibilities in section 3.4 favors possibility (c). These results are best understood by comparing the electronic situations in BLM and cytochrome P450.

**Comparison of ABLM and Cytochrome P450.** Compound I in heme chemistry is described as an  $\text{Fe(IV)}=\text{O}$  species and

(106) (a) Chang, C. H.; Dallas, J. L.; Meares, C. F. *Biochem. Biophys. Res. Commun.* **1983**, *110*, 959. (b) Chang, C. H.; Meares, C. F. *Biochemistry* **1982**, *21*, 6332. (c) Chang, C. H.; Meares, C. F. *Biochemistry* **1984**, *23*, 2268. (d) Xu, R. X.; Nettesheim, D.; Otvos, J. D.; Petering, D. H. *Biochemistry* **1994**, *33*, 907. (e) Xu, R. X.; Antholine, W. E.; Petering, D. H. *J. Biol. Chem.* **1992**, *267*, 944. (f) Xu, R. X.; Antholine, W. E.; Petering, D. H. *J. Biol. Chem.* **1992**, *267*, 950. (g) Otvos, J. D.; Antholine, W. E.; Wehrli, S.; Petering, D. H. *Biochemistry* **1996**, *35*, 1458. (h) Mao, Q.; Fulmer, P.; Li, W.; DeRose, E. F.; Petering, D. H. *J. Biol. Chem.* **1996**, *271*, 6185.

(107) Burger, R. M.; Horwitz, S. B.; Peisach, J. *Biochemistry* **1985**, *24*, 3623.



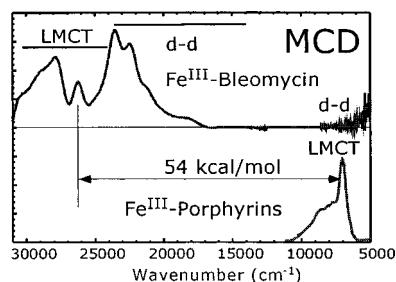


**Figure 12.** Comparison of MCD spectra for Fe(III)BLM and a prototype ferric heme (adapted from ref 108c) and demonstration of the large difference in LMCT energies.

a porphyrin radical. In cleaving the O—O bond one electron derives from the iron and one from the porphyrin ligand. Extended to BLM, this implies that if extensive delocalization occurs, that is, between the deprotonated amide and the pyrimidine, it would be expected that FeBLM could indeed form a high-valent compound I analogue of heme centers. This species would likely be highly reactive in hydrogen abstraction chemistry. However, the analysis in section 3.4.1 suggests that such a species does not form in BLM on energetics grounds. The main difference between BLM and cytochrome P450 is that in the latter the hole on the ligand is easily created and is delocalized over the whole porphyrin ring, whereas in BLM the hole is high in energy and localized on the deprotonated amide (see Figure 10). Delocalization of the hole over the deprotonated amide and the pyrimidine  $\pi$ -systems does not occur. Thus, there is very little stabilization of the ligand hole, and consequently the energetics of the heterolytic cleavage reaction are unfavorable for BLM.

This conclusion can be intuitively understood from Figure 12 where the MCD spectra of low-spin Fe(III)BLM and a low-spin Fe(III)–porphyrin are compared. Low-spin ferric porphyrins are known for showing prominent bands in the near-IR MCD spectra.<sup>108</sup> These bands, which were extensively used to identify axial ligands in hemoproteins, are assigned to LMCT transitions from the porphyrin ring into the  $t_{2g}$  hole on the iron.<sup>108</sup> The fact that these CT bands occur at very low energy reflects the ease of removal of an electron from the porphyrin ring. In sharp contrast, the MCD spectrum of Fe(III)BLM that was extensively analyzed in this study shows that the first LMCT transition is at  $\sim 25\,000\text{ cm}^{-1}$  in the near-UV region of the spectrum. The difference between these transition energies ( $\sim 18\,500\text{ cm}^{-1}$ ) is an experimental measure of how much harder it is to remove an electron from the BLM ligand compared to a porphyrin ring. Electronically this arises because the hole on the ligand is localized on the deprotonated amide, while in low-spin ferric porphyrins it is delocalized over the whole porphyrin ring. As indicated in Figure 12 the difference in ligand hole energies already accounts for  $\sim 54\text{ kcal/mol}$  difference in the heterolytic cleavage energetics of BLM versus cytochrome P450. In addition to this dominant electronic structure contribution to reactivity, two other factors should be mentioned that also contribute to this difference. First the total charge in the transition from peroxy P450 to compound I changes from  $-1$  to  $0$  in the case of cytochrome P450 but from  $0$  to  $+1$  for BLM. Because the neutral state is favored in enzyme active sites which

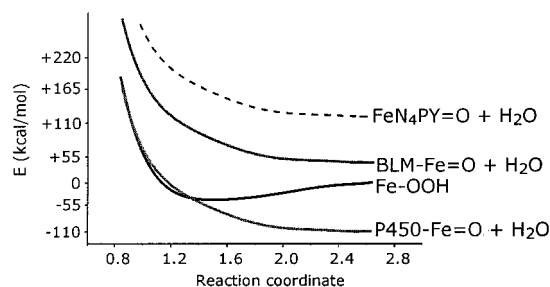


**Figure 13.** Qualitative potential energy surfaces for the heterolytic cleavage of the O—O bond in ABLM, cytochrome P450, and a non-heme iron–hydroperoxo complex.

have a low dielectric constant, this would also help to drive the heterolytic bond cleavage in cytochrome P450. Second the soft, strongly electron-donating thiolate axial ligand in cytochrome P450 certainly helps to stabilize high-valent states of the iron in contrast to BLM where no such soft donor ligand is present.

The barrier for the heterolytic cleavage reaction is dependent on the force constant of the peroxide bond and the energetics of the reaction. In Figure 13 qualitative potential energy surfaces (PESs) for the heterolytic cleavage of the O—O bond in ABLM and cytochrome P450 are plotted. The reaction coordinate in this case will have contributions mainly from O—O bond elongation and Fe=O bond shortening and, to a lesser extent, from rearrangement of the ligands and the surrounding solvent. The curve labeled “Fe—OOH” shows the bound state of the hydroperoxide. Protonation of the FeOOH produces the Fe—OOH<sub>2</sub> species that has no minimum on the potential energy surface and dissociates into the compound I analogue and water (remaining traces). If the thermodynamics of the reaction are highly favorable as for cytochrome P450 (P450=O + H<sub>2</sub>O), the crossing of the hydroperoxide bound surface and the dissociative surface occurs close to the equilibrium nuclear configuration of the hydroperoxo species. Consequently, the bond will easily break. A completely different situation exists for ABLM (BLM-Fe=O + H<sub>2</sub>O). Here the thermodynamics of the reaction are unfavorable, no crossing of potential energy surfaces occurs, and the reaction will have an exceedingly high activation barrier. Also included in Figure 13 is the trace labeled “FeN<sub>4</sub>PY=O + H<sub>2</sub>O”, which refers to the hypothetical O—O bond cleavage reaction of a recently reported hydroperoxo complex and that will be studied in detail in a forthcoming publication.<sup>93</sup> Here the energetics are even more unfavorable than for ABLM because the hole is produced on the very innocent ligand and thus is even higher in energy, a situation that is probably appropriate for other non-heme environments.

**H-Atom Abstraction Model.** The alternative to heterolytic bond cleavage in ABLM that was developed in this study is the direct attack of the substrate C—H bond by the hydroperoxide in ABLM. Such a reaction will have a very complicated PES. However, qualitative arguments favor the feasibility of this mode of action of BLM chemistry. The peroxide in ABLM is fairly electrophilic with a weak O—O bond due to a low-lying  $\sigma^*$  orbital caused by the protonation. Approach of the C—H bond would thus lead to electron transfer from the substrate to the peroxide, which would weaken both the C—H and the O—O bonds (Figure 11). This could lead to facile breakage of both bonds to produce water, a DNA radical, and the Fe(IV)BLM=O species. The overall reaction is envisioned to be energetically relatively close to neutral and could therefore proceed at ambient conditions. While direct experimental evidence for this model is lacking, it is an attractive working hypothesis.

(108) (a) Williams, R. J. P. *Chem. Rev.* **1956**, *5*, 299. (b) Cheng, J. C.; Osborne, G. A.; Stephens, P. J.; Eaton, E. A. *Nature (London)* **1973**, *241*, 193. (c) Cheesman, M. R.; Greenwood, C.; Thomson, A. J. *Adv. Inorg. Chem.* **1991**, *36*, 201. (d) Day, P.; Smith, D. W.; Williams, R. J. P. *Biochemistry* **1967**, *6*, 1563, 3747. (e) Makinen, M. W.; Churg, A. K. In *The Porphyrins*; Gray, H. B., Lever, A. B. P., Eds.; Addison-Wesley: Reading, MA, 1983; Vol. 1, p 141.

**Acknowledgment.** Our research is supported by the National Institute of Health (GM40392). F.N. acknowledges a post-doctoral fellowship from the Deutsche Forschungsgemeinschaft and Professor Peter Kroneck (Konstanz) for support during the final stages of manuscript preparation. Dr. Elna Pidcock is acknowledged for help with the resonance Raman experiments, and Dr. Nicolai Lehnert, for help with the electronic structure calculations. We also thank Jyllian Kemsley for a critical reading of the manuscript.

**Supporting Information Available:** EPR spectra and simulations for ABLM and Fe(III)BLM, ligand field analysis for ABLM, calculated vibrational frequencies for amide derivatives, calculated ABS spectra for different ABLM models (PDF). This material is available free of charge via the Internet at <http://pubs.acs.org>.

JA001812Y